Title
Diffusion MRI Methods for Improved Treatment Monitoring in Breast Cancer

Author
Aliu, Sheye

Publication Date
2009

Peer reviewed|Thesis/dissertation

Diffusion MRI Methods for Improved Treatment Monitoring in Breast Cancer

by

Sheye Oluwaseun Aliu

A dissertation submitted in partial satisfaction of the

requirements for the degree of

Joint Doctor of Philosophy
with the University of California, San Francisco

in

Bioengineering

in the

Graduate Division

of the

University of California, Berkeley

Committee in charge:

Professor Nola M. Hylton, Chair
Professor Steven M. Conolly
Professor Marian C. Diamond

Fall 2009

Diffusion MRI Methods for Improved Treatment Monitoring in Breast Cancer

by Sheye Oluwaseun Aliu

Abstract

Diffusion MRI Methods for Improved Treatment Monitoring in Breast Cancer

by

Sheye Oluwaseun Aliu

Joint Doctor of Philosophy in Bioengineering
with the University of California, San Francisco

University of California, Berkeley

Professor Nola M. Hylton, Chair

As of the time of this writing, the gold standard for monitoring primary breast tumor response to chemotherapy treatment is clinical examination based on palpable changes in tumor size. This method is non–quantitative, highly subjective and generally imposes that treatment is completed before efficacy can be assessed, defeating the purpose of monitoring and eliminating the prospect of adaptive treatment.

MRI methods including tissue enhancement kinetics are increasingly used to provide improved monitoring of treatment response in breast and other cancers. In this work, I investigate the added value of diffusion weighted imaging, an MRI technique, for treatment monitoring in breast cancer. This investigation was first conducted in a thoroughly characterized animal model of breast cancer and subsequently in breast cancer patients.

I furthered this work by exploring the potential benefit of diffusion tensor imaging, an MRI technique relatively novel to breast imaging, for breast cancer treatment monitoring. To achieve this, I developed a facile MRI protocol which was also used to study the effect of modulating diffusion time on diffusion measurements.

I found that diffusion weighted imaging parameters were sensitive to treatment induced changes both in an animal model of breast cancer and in breast cancer patients. Diffusion tensor imaging parameters were able to distinguish normal breast tissue from breast cancer but modulating the diffusion time did not result in any significant changes in diffusion measurements.

Contents

List of Figures

List of Tables

Acknowledgements

A great many people have contributed to this moment and I would like to express my sincerest appreciation. I hesitate to mention names lest I inadvertently omit anyone, but the following people are deserving of particular commendation:

My family for sustained encouragement and support when it mattered most.

My dissertation advisor Nola Hylton, whose mentorship over the years has made me into a better scientist and is reflected on every page of this dissertation.

Members of my qualifying exam committee: Roland Henry for multiple Socratic sessions on the fundamentals of diffusion MRI and constructive criticism at every turn; John Kurhanewicz for sage advice on procedural aspects of my project; Bonnie Joe for helping me embrace the clinical ramifications of my project.

Members of my dissertation committee, who also served on my qualifying exam committee. Steve Conolly for making sure I never lost sight of the big picture. Marian Diamond for excellent instruction in human anatomy and editing this document.

Members, past and present, of the Breast MRI Research Program at UCSF, who provided me with untold assistance in coordinating patient and volunteer studies.

Past and present faculty of the Joint Graduate Group in Bioengineering at UC Berkeley and UCSF, whose labs I rotated through: Srikantan Nagarajan for his mentorship and guiding me through my first peer-reviewed publication; Thomas Ferree for patiently inducting me to graduate research.

Above all, endless gratitude goes to the patients and volunteers who tolerated countless hours of MRI scans in the name of science.

Funding support was primarily provided by the National Institute of Health (RO1 CA059487).

Chapter 4 is adapted from an article published in *Journal of Magnetic Resonance Imaging* (Aliu et al., 2009).

CHAPTER 1

Introduction

Recent statistics from the American Cancer Society reveal that breast cancer mortality rates in the United States continue to decline by about 2% annually as they have since 1990 [1]. Similar trends have been reported in other industrialized regions [2]. This decline has been attributed to a combination of factors including improved awareness, broader screening efforts leading to earlier stage diagnosis and advances in treatment. While such modest improvements represent motion in the right direction, breast cancer remains the second leading cause of cancer deaths in women (behind lung cancer) and is the most common cancer among women, excluding non-melanoma skin cancers. Breast cancer treatment options vary according to a host of factors including history, phenotype and the stage at detection. The current gold standard for monitoring response to primary tumor treatment is clinical examination based on palpable changes in tumor size. Limitations of this standard include the fact that it is subjective and often relies on the completion of treatment. It is likely that the ability to monitor early response to treatment will play a role in further improving breast cancer mortality rates.

MRI methods have demonstrated greater accuracy in representing size and extent of breast tumors than current methods and have further shown promise in predicting response to treatment using tissue enhancement kinetics. The present work investigated the added value of diffusion weighted imaging (DWI) and the potential benefit of diffusion tensor imaging (DTI) in the context of breast cancer treatment monitoring.

In summary, the following work was completed:

- Pre-clinical: a mouse model of breast cancer was thoroughly characterized and subsequently applied towards investigating the added value of DWI in the context of monitoring response to breast cancer treatment.
- Clinical: a facile diffusion MRI protocol was developed and subsequently used to study the added value of DWI and the potential benefits of DTI in the context of monitoring response to breast cancer treatment in human subjects.

1.1 Chapter Organization

Chapters in this work are organized as follows:

Chapter 2	General breast cancer overview, including relevant statistics and current strategies for detection, diagnosis and treatment.
Chapter 3	Overview of MRI, including fundamental physics and guiding principles of DWI, DTI and contrast enhanced MRI.

Chapter 4	A pre-clinical study examining whether MRI parameters are sensitive to the effects of targeted therapy and the ability of DWI parameters to add value to more traditional MRI parameters, in the context of treatment monitoring.
Chapter 5	A clinical study characterizing normal fibroglandular breast tissue and breast cancer, investigating the added value of DWI and the potential benefit of DTI in the context of monitoring breast cancer treatment.
Chapter 6	Summary of findings, reflection on limitations and discussion of future directions.

1.2 References

1. *Breast Cancer Facts & Figures 2007-2008*. 2007, American Cancer Society, Inc.: Atlanta.
2. Mettlin, C., *Global Breast Cancer Mortality Statistics.* CA Cancer J Clin, 1999. **49**(3): p. 138-144.

CHAPTER 2

Breast Cancer Overview

This chapter provides an overview of breast anatomy and breast cancer, including relevant statistics and current strategies for detection, diagnosis and treatment.

2.1 Breast Anatomy

2.1.1 Gross Structure

Sir Astley Cooper is generally credited with first studying the anatomy of the human breast in 1840 [1]. Using dissections from previously lactating female cadavers, Cooper described the breast as a gland comprised of external components (nipple, areola, tubercles and some glands) and internal components (secretory glandules connected to the nipple by lactiferous ducts). Cooper reports that " … the glandules and ducts are united to each other by a fibrous and inelastic membrane which penetrates the surface of the gland [breast], and sends fibers to all of its interstices and by uniting its small constituent glandulous bodies, forms it into what is called a conglomerate gland" [1]. He also describes a cellular membrane where an abundance of fat is deposited, arteries, veins, absorbents and nerves hold their course, and are distributed to the substance of the gland and its appendage the nipple [1].

Contemporary knowledge corroborates some of Cooper's work. It is currently held that the breast is an apocrine gland consisting mainly of lobules (milk producing glands) aggregated into lobes, ducts (which transport milk from the lobules to the nipples) and stroma (fatty tissue and connective tissue surrounding the ducts and lobules, blood vessels, and lymphatic vessels).

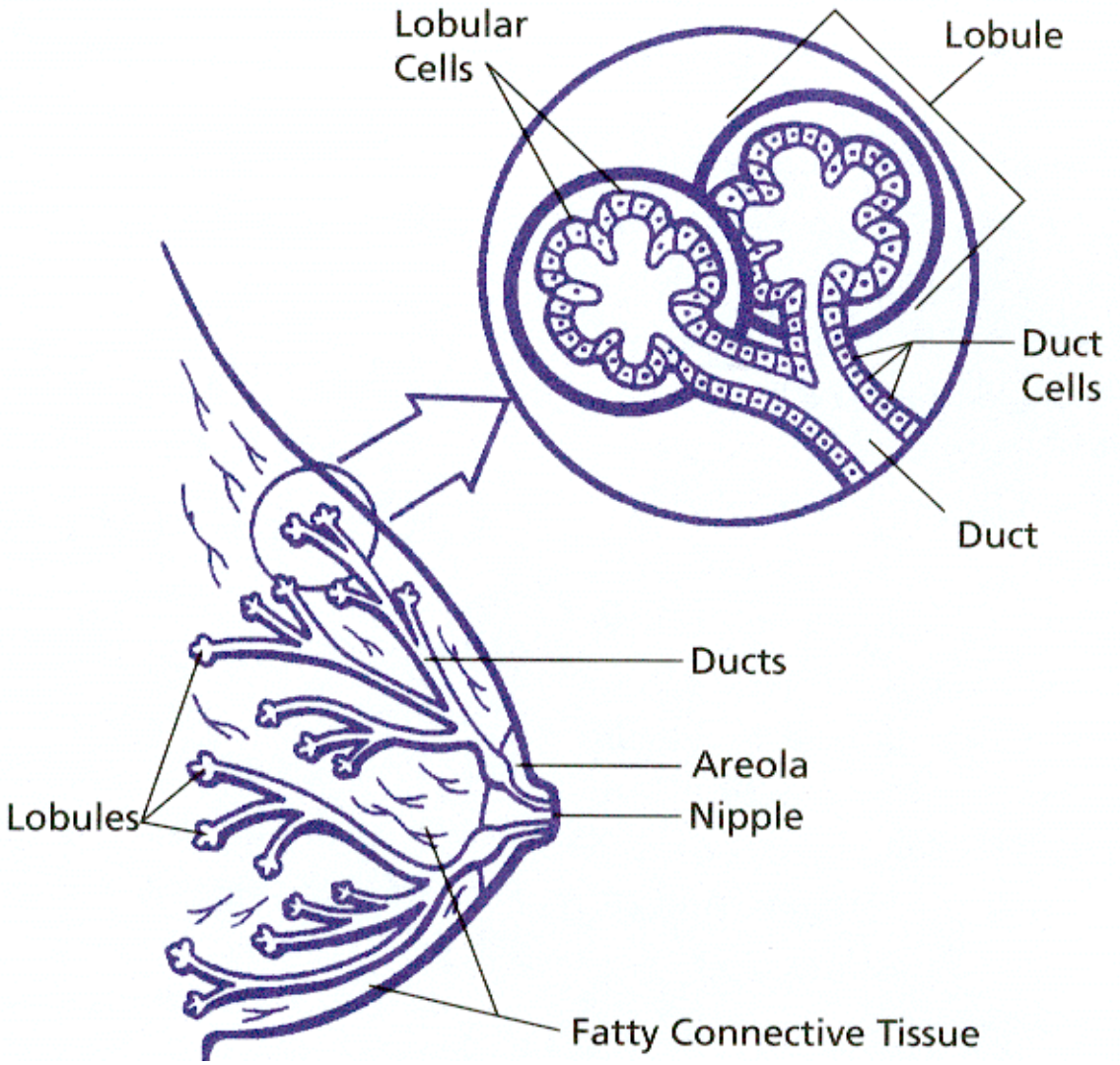

Figure 2.1 Illustration of breast anatomy. The nipple protrudes externally from the anterior surface of the breast and is surrounded by the areola. Lactiferous ducts converge on the nipple. Internally, the breast is comprised of lobules and connecting ducts which are aggregated into lobes. These tissues are surrounded by fatty connective tissue.

The mammary region contains the two breasts or mammary glands, situated on opposite sides of the thorax. The breasts sit on the fore part of the pectoralis major, between the sternum and the axilla and generally extend from the level of second rib to the level of the sixth rib anteriorly. From the anterior surface of the breast projects the nipple or mamilla. Each nipple is surrounded by the areola, a dark circular layer, which ranges in color from pink to dark brown and features several glands.

Arterial supply to the breast derives from the internal thoracic artery, lateral thoracic artery, thoracoacromial arteries and posterior intercostal arteries, while venous drainage is primarily through the axillary vein with some drainage through the internal thoracic vein and the intercostal veins. The breast is innervated by the anterior and lateral cutaneous branches of the fourth through sixth intercostal nerves [2].

Lobes, Lobules and Acini

Each breast is organized into lobes which converge on the nipple through a system of overlapping ducts. The number of lobes has been reported in the range 15-25 [3-5]. Approximately two-thirds of the breast lobes are situated within 30 mm of the base of the nipple [6]. Each lobe is comprised of lobules connected together by ducts. Lobules are themselves comprised of clusters of acini.

Ducts

The nature of breast ducts and their number has enjoyed some controversy. Early work by Cooper [1] which served as a canon for many years was based on wax casting which unfortunately biased his conclusions. Most notably, Cooper injected wax into the ducts at the nipple opening and arranged them in ordered fashion for an artist rendition.

Figure 2.2 A wax cast of the lactating breast developed by Sir Astley Cooper. Cooper formulated his cast by laying out the ducts relatively homogenously and injecting colored wax into the duct openings at the nipple. This procedure inadvertently inflated those ducts, giving the false impression that ducts expand near the nipple into so called lactiferous sinuses. Cooper's layout was erroneously duplicated in several anatomy texts. Image reproduced from [1].

Consequentially, Cooper reported that ducts possess lactiferous sinuses (milk collecting sacs) near the nipple and his ordered arrangement of the ducts was pervasively reproduced in anatomy textbooks. It is now accepted that the network of ducts in the breast is not homogenous but complex and that lactiferous sinuses are merely an artifact of Cooper's wax injection process and do not in fact exist [6].

Between 4 and 18 ducts, also known as lactiferous ducts, exit the nipple with an average mean diameter of 2 mm at the base of the nipple [6]. Measured posteriorly beginning at the nipple, ducts begin branching after about 7 mm, first into lobes, then further into lobules and finally into acini.

Tissues of the Breast

The glandular tissues of the breast are surrounded by connective tissue (collagen and elastin), adipose tissue (fat) and suspensory fibers termed Cooper's ligaments. The volumetric composition of the breast changes markedly with age and pregnancy. The ratio of glandular tissue to fatty tissue rises from about 1:1 in the non-lactating breast to about 2:1 in the lactating breast [6].

2.1.2 Ultrastructure

A comprehensive histology of breast tissues is beyond the scope of this chapter as the state of these tissues is not constant and changes with the menstrual cycle, pregnancy, lactation and menopause. What follows is a brief overview of the histology of tissues in the normal non-lactating breast.

The primary anatomical and functional unit of the breast is the terminal ductal lobular unit (TDLU), which as the name suggests is the terminal portion of the lactiferous duct (internal to the nipple) and its lobular branches. The TDLU is the basic reacting unit in the human breast and most forms of breast cancer arise from the epithelium of the TDLU. For purposes of microscopic illustration, the nomenclature developed by Wellings et al [7] is adopted in describing the TDLU. Namely, ducts connecting lobules are denoted as extralobular terminal duct (ETD) and ducts connecting acini (A) within the lobule are denoted as intralobular terminal duct (ITD).

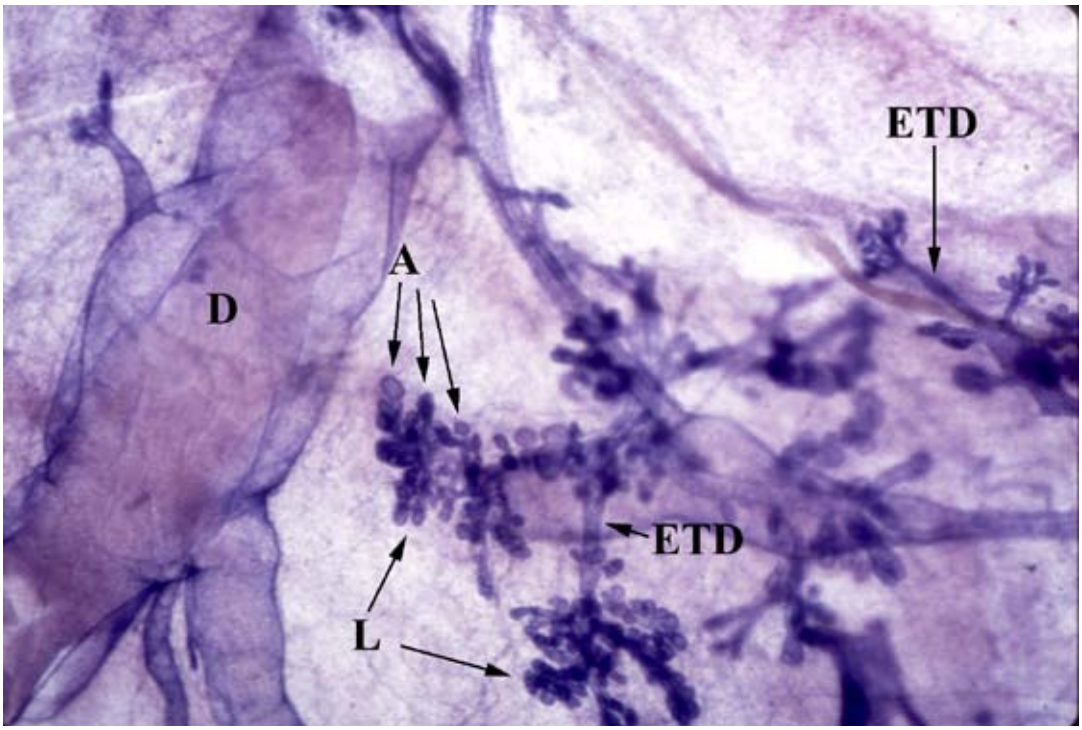

Figure 2.3 Slide (Hematoxylin stain) showing a group of TDLUs. Highlighted are a dilated duct (D), several acini (A) connected to a lobule (L) and extralobular terminal ducts (ETDs) connecting lobules. Each lobule measures about 1 mm in diameter. Image reproduced from [7].

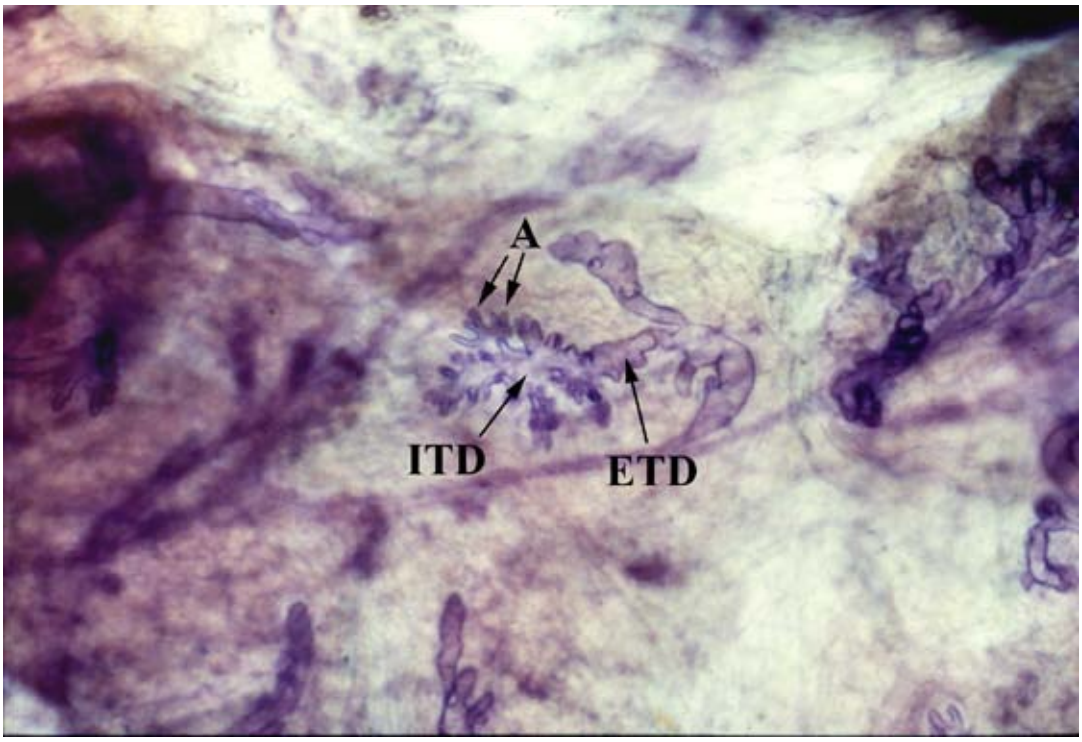

Figure 2.4 Slide (Hematoxylin stain) of a TDLU measuring about 1.5 mm long by 1.0 mm wide. Highlighted are a pair of acini (A), an Intralobular terminal duct (ITD), i.e. the axial space in the lobule and an extralobular terminal duct (ETD). Image reproduced from [7].

The ducts of the breast generally possess an inner layer (luminal) of epithelial cells and a moderately discontinuous outer layer (basal) of myoepithelial cells . The epithelial layer is comprised of cuboidal or columnar cells in lobular ducts (ITD), pseudostratified columnar cells in extralobular ducts (ETD) and squamous cells proximal to the nipple [8]. The acini (A) are lined by cuboidal epithelium and also contain lactocytes (mammary secretory epithelial cells).

2.2 Breast Cancer Demographics

Breast cancer is the second leading cause of cancer deaths among women today (behind lung cancer) and is the most common malignancy among women, excluding non-melanoma skin cancers. The American Cancer Society estimates that about 1.3 million women worldwide are diagnosed annually with breast cancer and about 465,000 will die from the disease [9].

2.3 Breast Cancer Symptoms

Early breast cancer can be asymptomatic but as tumors develop, common physical symptoms can include:

- lumps in the breast or armpit
- changes to the size, shape, or feel of the breast or nipple — such as tenderness, scaliness or dimpling

- spontaneous nipple discharge

2.4 Breast Cancer Risk Factors

2.4.1 Gender

Gender is the main risk factor for developing breast cancer as women are purportedly 100 times more likely to develop breast cancer than men are.

2.4.2 Age

Following gender, age is the most important factor affecting breast cancer risk.
Close to 80% of breast cancers occur in women older than age 50.

2.4.3 Family and Personal History

A family history of breast cancer impacts breast cancer risk: having one first-degree relative (mother, sister, or daughter) with breast cancer approximately doubles a woman's risk and having two first-degree relatives increases risk about five-fold. Personal history of breast cancer also impacts breast cancer risk: a woman with cancer in one breast has an increased risk of developing a new cancer in the other breast or in another part of the same breast, separate from a recurrence.

2.4.4 Genetic Predisposition

Inherited genetic mutations in several genes notably the BRCA1 and BRCA2 genes increase the risk of developing breast and other cancers. Defects in other genes such as ATM, CHEK2, p53 and PTEN also impart increased breast cancer risk.

2.4.5 Dense Breast Tissue

Evidence shows that women with denser breast tissue (a high proportion of lobular and ductal tissue) have a higher risk of developing breast cancer relative to women with more fatty breast tissue. Dense breast tissue can also make mammographic detection of cancer more challenging.

2.4.6 Exposure to Hormones

Studies show that the longer a woman is exposed to estrogen (such as through uninterrupted menstrual cycles), the more likely she is to develop breast cancer. Risk is therefore increased among women who experience early menarche, late menopause, have their first child late, never have children or take hormone replacement therapy for extended periods of time.

2.4.7 Personal History of Breast Radiation

Previous radiation treatment to the chest area (such as treatment during youth or treatment for another cancer type) increases the risk of developing breast cancer. Risk is greatest if radiation treatment was received as an adolescent during breast development.

2.4.8 Excessive Use of Alcohol

The American Cancer Society estimates that women who drink more than one alcoholic beverage a day have about a 20% greater risk of breast cancer than do women who do not drink.

2.5 Breast Cancer Types

Upwards of 85% of breast cancers are ductal in origin, few are lobular and even fewer begin in other tissues of the breast.

2.5.1 In situ Breast Cancer

In situ (noninvasive) breast cancer refers to individual cells with malignant changes that have not infiltrated any surrounding breast tissue, remaining in their place of origin within the ducts (ductal carcinoma in situ or DCIS) or lobules (lobular carcinoma in situ or LCIS).

2.5.2 Invasive Breast Cancer

Invasive (infiltrating) breast cancers are cancers that have spread outside the basement membrane of the ducts (invasive ductal carcinoma or IDC) or lobules (invasive lobular carcinoma or ILC) and have invaded surrounding breast tissue.

2.5.3 Less Common Breast Cancers

Less common types of breast cancer can arise from supporting tissue of the breast such as fibrous connective tissue, blood vessels and the lymphatic system. Unusual types of breast cancer include inflammatory breast cancer, phyllodes tumor, angiosarcoma, osteosarcoma, metaplastic breast cancer, adenoid cystic carcinoma and Paget's disease of the breast. There are also rare subtypes of invasive ductal carcinoma — tubular, mucinous, medullary and papillary [10].

2.6 Breast Cancer Staging

Staging is the process used to evaluate the magnitude and extent of tumors and is a major consideration in selecting treatment options and determining prognosis. The internationally accepted TNM system considers *tumor* size and spread to surrounding tissue (T), lymph *node* involvement (N) and *metastasis* to distant sites (M) in classifying tumors [11, 12]:

Stage	Tumor Size	Lymph Node Involvement	Metastasis
Stage 0	In situ	No	No
Stage 1	Less than 2 cm	No	No
Stage 2A	None apparent	Regional, but nodes are movable	No
	Less than 2 cm	Regional, but nodes are movable	No
	Between 2-5 cm	No	No
Stage 2B	Between 2-5 cm	Regional, but nodes are movable	No
	Greater than 5 cm	No	No
Stage 3A	None apparent	Regional, nodes are non-movable	No
	Less than 2 cm	Regional, nodes are non-movable	No
	Between 2-5 cm	Regional, nodes are non-movable	No
	Greater than 5 cm	Regional	No
Stage 3B	Extends to chest/skin	Yes; any node	No
Stage 3C	Any size and extends	Yes; internal mammary	No
Stage 4	Any size and extends	Yes; any node	Yes

Table 2.1 Breast cancer staging according to the TNM system which categorizes cancers based on *tumor* size and spread to neighboring tissue (T), lymph *node* involvement (N) and *metastasis* to distant sites (M). Note that inflammatory cancer, a rare invasive cancer, is generally categorized as Stage 3B.

2.7 Breast Cancer Detection

Breast cancer screening is traditionally accomplished by breast exam (self or clinician administered), mammography or ultrasound. MRI is gaining ground as an accepted screening tool among high risk women.

2.7.1 Clinical Breast Exam

Breast exam involves visual inspection and palpation of the breasts. This method is subjective, leading to varied results depending on the examiner and is prone to overestimating actual tumor size.

2.7.2 Mammography

Mammograms are by far the most common breast cancer screening tool. Mammography uses low energy x-rays to examine the compressed breast. Contrast in mammography results from differences in the absorption or attenuation of x-rays by different tissues in the breast. The

sensitivity of mammography to breast cancer has been reported to range from 63% to 98% [13, 14] and as low as 30%–48% in radiographically dense breasts [15, 16]. Limitations of mammography include difficulty in distinguishing recurrent tumors from scar tissue in the postoperative breast [17] and inaccuracy in depicting size and extent of masses especially when intraductal disease is present [18].

2.7.3 Ultrasound

Ultrasound, also called sonography, uses high frequency sound waves to penetrate breast tissue and measures the reflection signature from different tissues in the breast. Due to inability to consistently detect early signs of cancer such as microcalcifications, ultrasound is not routinely used for breast cancer screening but primarily to distinguish solid tumors from fluid filled cysts, evaluate suspected carcinomas in mammographically dense breasts and for biopsy guidance.

2.7.4 Magnetic Resonance Imaging

Magnetic Resonance Imaging (MRI) is emerging as a promising tool for screening breast cancer especially among high risk women. MRI has also demonstrated greater sensitivity in detecting small (less than 1 cm) lesions and succeeds in certain scenarios where other imaging modalities are challenged, such as imaging dense breasts, the post-operative breast and augmented breasts [19, 20]. Drawbacks of MRI include moderate diagnostic specificity and higher cost.

2.8 Breast Cancer Diagnosis

Biopsy is the only definitive way to determine whether a mass is malignant or benign. As such, abnormalities detected with any of the afore-discussed techniques might be queried by biopsy. Common forms of breast biopsy include fine needle aspiration (FNA), core biopsy, vacuum assisted biopsy and open surgical biopsy.

2.9 Breast Cancer Treatment

Breast cancer therapy comprises local treatments and systemic treatments and often a combination of both. Local treatments include surgery and radiation. The aim of local treatments is to eradicate the disease at source or the primary tumor. Systemic treatments such as chemotherapy and hormone therapy are generally directed against the spread of disease to other body regions. Local treatment suffices for some patients but breast cancer mortality is typically associated with systemic disease spread. As such, patients at risk of systemic disease spread are treated with both local and systemic therapies.

2.9.1 Local Treatments

Surgery remains a tried and true defense against breast cancer. Traditionally, radical mastectomy (removing the entire breast, the axillary lymph nodes, and the pectoralis major and minor

muscles behind the breast) was routine treatment for breast cancer. However, this practice is disfiguring and can be traumatic for patients despite elective follow-up reconstructive surgery. Additionally, radical mastectomy can be disruptive to the lymph system, presenting post surgery complications. There has been a paradigm shift towards breast conserving surgery, otherwise known as lumpectomy, whenever possible. Unlike mastectomy where the entire breast is removed, lumpectomy is designed to remove a discrete tumor lump and a surrounding margin of normal tissue. This practice results in significantly less disfigurement but is typically reserved for women with smaller or localized tumors. Outcome studies in women with locally advanced breast cancer, comparing mastectomy to lumpectomy followed by radiation, show similar survival rates [21-24].

Similar to the paradigm shift towards breast conserving surgery, there has been a shift towards sentinel lymph node biopsies over full axillary lymph node removal in recent years. Like the name suggests, sentinel nodes are the first lymph node(s) in the tumor's path and can be identified by the injection of contrast media near the tumor region prior to surgery. If neoplasia is detected in the sentinel node(s), a full axillary dissection is typically performed for staging, otherwise full axillary dissection might be deemed unnecessary. Studies have shown sentinel node biopsy to be as effective in detecting disease spread as full axilla dissection. Sentinel node biopsy has the added benefit of being less disruptive to the lymphatic system [21, 22].

Radiation therapy also referred to as radiotherapy, is a highly targeted approach to treating cancer, using high energy x-rays to kill cancer cells. Radiotherapy is typically administered as adjuvant therapy post surgery, targeting any residual cancerous cells in the tumor region after surgery. Radiation is debilitating to cellular DNA, leading to cell mutations and ultimately cell death. While radiation preferentially impacts rapidly dividing cancer cells, it also affects normal cells. Hence great precaution is undertaken to ensure radiation is only focused on cancerous tissue. Radiation is most commonly delivered externally, via a linear accelerator. It is also possible to deliver radiation internally by implanting radioactive pellets directly into malignant tissue.

2.9.2 Systemic Treatments

Chemotherapy is primarily used to combat the systemic spread of disease. Chemotherapy typically involves a combination of cytotoxic drugs and is commonly administered intravenously. Drugs enter the bloodstream and travel through the body, killing off malignant cells by impairing cell multiplication. Common side effects of chemotherapy result from the fact that chemotherapy can also affect normal rapidly dividing cells such as cells in the intestinal tract, nails and hair. This explains often reported symptoms of nausea, nail and hair loss during treatment.

Hormonal therapy is used to deny cancer cells the hormones that promote their growth in a subset of breast cancers. Female hormones, estrogen and progesterone, can promote the growth of certain cancers. Cancers that possess estrogen or progesterone receptors, also referred to as estrogen receptor positive (ER+) and progesterone receptor positive (PR+) cancers, may benefit from selective modulators which bind to these receptors, blocking the action of hormones.

2.10 Monitoring Response to Chemotherapy

The current standard for evaluating primary breast tumor response to chemotherapy is clinical breast examination which entails breast palpation to estimate changes in tumor size. However this method is subjective and hardly quantitative. Pathologic response to chemotherapy as determined by residual tumor size at surgery has been demonstrated to be a better predictor of outcome than clinical breast examination [27-29] but requires that treatment is completed before treatment efficacy can be assessed. The task of monitoring treatment response is particularly challenging because mere changes in tumor size are not singularly decisive of prognosis. An ideal monitoring platform will, in addition to accurately representing changes in tumor size, incorporate information on tumor cellularity, vascularization and preferably predict tumor response to therapy as early as possible. Beyond accurately representing size and extent of breast lesions, MRI methods have demonstrated promising results in predicting tumor response by complementing changes in tumor size with tissue enhancement kinetics. The present work investigates the added predictive value of diffusion weighted MRI in monitoring treatment response and explores the potential benefit of diffusion tensor MRI in breast cancer.

2.11 References

1. Cooper, A.P., *On the Anatomy of the Breast*. 1840, London, UK: Longman, Orme, Green, Browne and Longmans.
2. Sarhadi, N.S., J. Shaw-Dunn, and D.S. Soutar, *Nerve Supply of the Breast With Special Reference to the Nipple and Areola: Sir Astley Cooper Revisited.* Clin Anat, 1997. **10**(4): p. 283-288.
3. Cheatle, G.L. and M. Cutler, *Tumors of the breast: Their pathology, symptoms, diagnosis and treatment*. 1931, London: Edward Arnold.
4. Page, D.L. and T.J. Anderson, *Diagnostic histopathology of the breast*. 1988, Edinburgh: Churchill Livingstone.
5. Tavassoli, F.A., *Pathology of the breast*. 1992, Norwalk, Connecticut: Appleton and Lange.
6. Ramsay, D.T., et al., *Anatomy of the lactating human breast redefined with ultrasound imaging.* J. Anat, 2005. **206**(6): p. 525-534.
7. Wellings, S.R., H.M. Jensen, and R.G. Marcum, *An atlas of subgross pathology of the human breast with special reference to possible precancerous lesions.* J Natl Cancer Inst, 1975. **55**(2): p. 231-273.
8. Stirling, J.W. and J.A. Chandler, *The fine structure of the normal, resting terminal ductal-lobular unit of the female breast* Arch A Pathol Anat Histol, 1976. **372**(3): p. 205-226.
9. *Breast Cancer Facts & Figures 2007-2008*. 2007, American Cancer Society, Inc.: Atlanta.
10. *Types of breast cancer*, in *MayoClinic.com*. 2007, Mayo Foundation for Medical Education and Research.
11. Beahrs, O.H., et al., *Manual for Staging of Cancer*. 1992, Philadelphia: J.B. Lippincott. 149-154.
12. Singletary, E., et al., *Revision of the American Joint Committee on Cancer Staging System for Breast Cancer.* Clin Oncol, 2002. **20**(17): p. 3628-3636.
13. Burhenne, H., et al., *Interval breast cancers in the Screening Mammography Program of British Columbia: analysis and classification* Am J Roentgenol, 1994. **162**(5): p. 1067-1071.
14. Kerlikowske, K., et al., *Effect of age, breast density, and family history on the sensitivity of first screening mammography.* J Am Med Assoc, 1996. **276**(1).
15. Mandelson, M.T., et al., *Breast Density as a Predictor of Mammographic Detection: Comparison of Interval- and Screen-Detected Cancers* J Natl Cancer Inst, 2000. **92**(13).
16. Kolb, T.M., J. Lichy, and J.H. Newhouse, *Comparison of the Performance of Screening Mammography, Physical Examination, and Breast US and Evaluation of Factors that Influence Them: An Analysis of 27,825 Patient Evaluations.* Radiology, 2002. **225**(1): p. 165-175.
17. Sickles, E. and K. Herzog, *Mammography of the postsurgical breast* Am J Roentgenol, 1981. **136**(3): p. 585-588.
18. Boetes, C., et al., *Breast tumors: comparative accuracy of MR imaging relative to mammography and US for demonstrating extent.* Radiology, 1995. **197**(3): p. 743-747.

19. Heywang, S., et al., *Gd-DTPA Enhanced MR Imaging of the Breast in Patients with Postoperative Scarring and Silicon Implants.* J Comput Assist Tomogr, 1990. **14**(3): p. 348-356.
20. Dao, T., et al., *Tumor recurrence versus fibrosis in the irradiated breast: differentiation with dynamic gadolinium-enhanced MR imaging.* Radiology, 1993. **187**(3): p. 751-755.
21. Giuliano, A.E., et al., *Prospective Observational Study of Sentinel Lymphadenectomy Without Further Axillary Dissection in Patients With Sentinel Node–Negative Breast Cancer* J Clin Oncol, 2000. **18**(13): p. 2553-2559.
22. Schrenk, P., et al., *Morbidity following sentinel lymph node biopsy versus axillary lymph node dissection for patients with breast carcinoma.* Cancer, 200. **88**(3): p. 604-614.

CHAPTER 3

MRI Methods for Monitoring Treatment Response in Breast Cancer

---

This chapter provides a brief review of fundamental MR physics and imaging principles and then reviews MRI methods used for monitoring treatment response in cancer.

3.1 MRI Fundamentals

3.1.1 Brief History

Magnetic resonance imaging (MRI) evolved from nuclear magnetic resonance (NMR) which has been in use by chemists and physicists since the 1940s. In 1973, Paul Lauterbur conducted the first MRI experiment by introducing gradients to the magnetic field, allowing for spatial localization of the NMR signal and leading to the acquisition of two dimensional images [1]. MRI has since been established as a safe non-invasive imaging modality capable of providing a wealth of information on the anatomy and physiology of the body. Magnetic resonance (MR) relies on the interaction between atoms and an external magnetic field. The nucleus of the atom is comprised of protons and neutrons, both of which intrinsically possess a quantum mechanical property known as spin. Protons and neutrons combine into the nucleus such that their spins cancel. Hence atoms with an odd number of protons or neutrons are said to posses net nuclear spin and are MR active. Hydrogen (^{1}H) is the most biologically abundant nucleus with net nuclear spin, on account of its single proton, and thus enjoys the greatest sensitivity to MR. Resultantly, most MR experiments are tuned to the resonant frequency of protons.

3.1.2 The Proton

Protons intrinsically possess nuclear spin, a property also referred to as nuclear angular momentum, which produces a magnetic moment about each proton

$$\boldsymbol{\mu} = \gamma \boldsymbol{J} \tag{3.1}$$

where $\boldsymbol{\mu}$ is the magnetic moment, γ is the gyromagnetic constant which has a value of 42.58 MHz/Tesla for protons and $\boldsymbol{J}$ is the spin angular momentum. Protons placed in an external magnetic field, $\boldsymbol{B}_0$, will tend to align the magnetic moment of their spins in parallel or anti-parallel with $\boldsymbol{B}_0$. Spins aligned parallel to $\boldsymbol{B}_0$ reside in a lower energy state E, relative to spins aligned anti-parallel to $\boldsymbol{B}_0$

$$E = \hbar \gamma m_s \boldsymbol{B}_0 \tag{3.2}$$

where $\hbar$ and γ are the reduced Planck's constant and the gyromagnetic constant respectively, and m_s indicates that the spin can inhabit one of two eigenstates, $\pm\frac{1}{2}$. Transition between both energy states requires the absorption of a photon with energy exactly equal to the energy difference between the energy states.

$$\Delta E = \hbar\gamma \boldsymbol{B}_0 \tag{3.3}$$

The ratio between spins parallel to the magnetic field and spins anti-parallel to the magnetic field is governed by the Boltzmann probability distribution

$$\frac{N_\downarrow}{N_\uparrow} = e^{\frac{-\Delta E}{kT}} \tag{3.4}$$

where $N_\downarrow$ is the spin population anti-parallel to the magnetic field, $N_\uparrow$ is the population parallel to the magnetic field, k is the Boltzmann constant and T is the absolute temperature. At room temperature the population of spins in the lower energy state, $N_\uparrow$, slightly exceeds the population of spins in the higher energy state, $N_\downarrow$, (about 7 in a million) which results in a slight polarization that underlies the MR phenomenon. The MR signal is thus proportional to the population difference between the energy states and is dependent on $\boldsymbol{B}_0$. The net magnetic moment of the excess of spins aligned parallel with $\boldsymbol{B}_0$ can be detected at equilibrium

$$\boldsymbol{M}_0 = \frac{\rho_0 \gamma^2 \hbar^2}{4kT} \boldsymbol{B}_0 \tag{3.5}$$

where $\boldsymbol{M}_0$ is the magnetization (net of all spin magnetic moments) and ρ_0 is the proton density.

3.1.3 Precession

In the presence of $\boldsymbol{B}_0$, the magnetization, $\boldsymbol{M}$, precesses about the axis of $\boldsymbol{B}_0$ according to the cross product of $\boldsymbol{M}$ and $\boldsymbol{B}_0$

$$\frac{d\boldsymbol{M}}{dt} = \gamma \boldsymbol{M} \times \boldsymbol{B}_0 \tag{3.6}$$

at a resonant frequency ω, the larmor frequency, estimated as

$$\omega = \gamma \boldsymbol{B}_0 \tag{3.7}$$

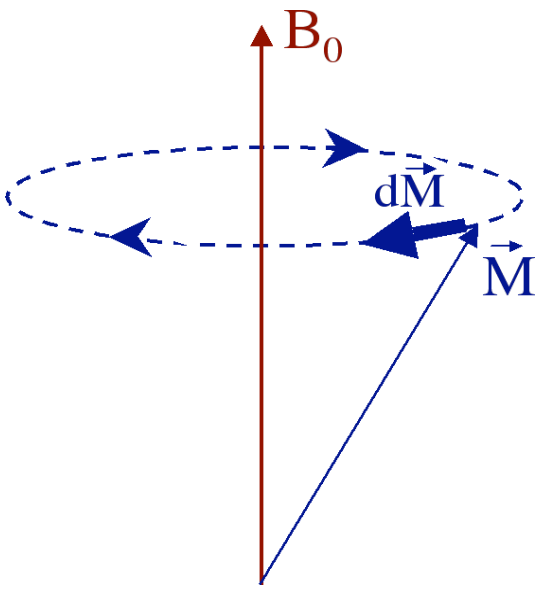

Figure 3.1 Precession of the magnetization (***M***) around an external magnetic field, $\boldsymbol{B}_0$, oriented in the *z* direction. Diagram reproduced from [2].

3.1.4 Excitation

An oscillating magnetic field—also referred to as a radiofrequency (RF) field—$\boldsymbol{B}_1$, rotating similarly to the precessing spins can be generated by an RF coil to excite the spins, establishing a coherent phase among the randomly precessing spins. The energy required for such excitation is the energy difference between the spin states and is achieved by setting the frequency of the oscillating field, $\boldsymbol{B}_1$, to the larmor frequency, ω. $\boldsymbol{B}_1$ is applied perpendicularly to $\boldsymbol{B}_0$, and induces a torque that rotates or tips ***M*** away from the static $\boldsymbol{B}_0$ onto a transverse plane. The rest of this chapter will assume for consistency that $\boldsymbol{B}_0$ is oriented longitudinally along the *z* axis and the corresponding transverse plane is oriented in the *xy* axis. The tipped component of ***M*** in the transverse plane, $\boldsymbol{M}_{xy}$, can be detected according to Faraday's law of induction [3]. The frequency of rotation away from $\boldsymbol{B}_0$ in the presence of $\boldsymbol{B}_1$ is estimated as

$$\omega_1 = \gamma \boldsymbol{B}_1 \tag{3.8}$$

The angle between the tipped ***M*** and $\boldsymbol{B}_0$ is referred to as the flip angle, α, and is estimated as

$$\alpha = \int_0^{\tau} \omega_1(t)dt \tag{3.9}$$

where τ is the duration of the RF pulse and is commonly chosen to yield a flip angle of 90° or 180°.

The RF coils used for excitation can also be used to detect the precessing transverse magnetization over the entire volume and this amounts to the recorded MR signal. The measured signal is called a free induction decay (FID) and may be transformed from its native time domain into the frequency domain by applying the Fourier transform [4]

3.1.5 Relaxation

$\boldsymbol{B}_1$ is typically applied for a few milliseconds at most, exciting spins into higher energy states after which the spins gradually lose their phase coherence and relax to equilibrium conditions. Relaxation results in a decay of the transverse magnetization and simultaneous regrowth of the magnetization along the longitudinal axis. Relaxation rates are influenced by factors such as local molecular structure, inter-molecular interactions and extra-molecular interactions with the external environment, referred to as the lattice. MRI exploits the fact that different tissue intrinsically exhibit different relaxation times, to generate contrast.

The Bloch equation describes the time dependent magnitude of $\boldsymbol{M}$, accounting for precession and relaxation

$$\frac{\partial \boldsymbol{M}(t)}{\partial t} = \gamma \boldsymbol{M}(t) \times \boldsymbol{B} + \frac{1}{T_1}\left(\boldsymbol{M}_0 - \boldsymbol{M}_z(t)\right) - \frac{1}{T_2}\boldsymbol{M}_{xy}(t) \tag{3.10}$$

where $\boldsymbol{M}_z$ is the longitudinal magnetization, T_1 is the spin-lattice relaxation time constant that describes the time required for the magnetization to regrow to 63% of its initial value along the longitudinal axis and T_2 is the spin-spin relaxation time constant that describes the time required for the transverse magnetization to decay to 37% of its value following RF pulsing.

T_1 relaxation results from protons losing energy in exchange with the lattice which efficiently occurs when protons are rotating at the larmor frequency. T_2 relaxation results from a broadening of resonant frequencies and subsequent loss in phase coherence of the transverse magnetization. Motion of protons and local field inhomogeneities can induce faster dephasing of the transverse magnetization and thus shorter T_2 relaxation times. Local magnetic heterogeneity effectively creates spatial gradients across a volume, broadening resonant frequencies and exacerbating the loss of phase coherence of the transverse magnetization. This additional dephasing relative to T_2 relaxation, constitutes a phenomenon known as T_2* decay [5]. Unlike T_2 relaxation which is an intrinsic phenomenon, T_2* decay is reversible [6, 7].

3.16 Signal Localization

MR images are essentially snapshots of the amplitude of the transverse magnetization across a sample at a particular time. Exploiting the fact that the resonant frequency is directly proportional to the magnetic field, it is possible to alter the magnetic field in a controlled manner such that it varies linearly along a particular axis, forcing the corresponding resonant frequency of spins to vary linearly with position along that axis. Altering the magnetic field is achieved by applying a much smaller linearly varying magnetic field, known as a ‘gradient field’. The differential resonant frequency of spins at different locations in the gradient field can be expressed as

$$\omega(z) = \omega_0 + \Delta\omega(z) = \gamma(B_0 + G_z z) \tag{3.11}$$

where G_z denotes the gradient field strength along the z direction. Such use of gradients to establish a relation between the position of spins and their frequency of precession is referred to as ‘frequency encoding’. A similar strategy, ‘phase encoding’, involves applying a gradient for some duration to produce phase variation across a sample. The integral of the gradient field

multiplied by $\frac{\gamma}{2\pi}$ is known as the spatial frequency variable, denoted *k*. Stepping through varying gradient field strengths produces different *k* values which collectively comprise *k* space.

For imaging purposes, an RF pulse in conjunction with a gradient field can be used to singularly excite spins within a specific frequency band. The region to be imaged—henceforth referred to as a slice—is selected according to the center frequency and bandwidth (range of frequencies) of the RF pulse, and the gradient field strength

$$\Delta z = \frac{\Delta \omega}{\gamma G_z} \tag{3.12}$$

Following slice selection, the transverse magnetization is further localized by applying additional gradients known as 'phase encoding gradients' along a perpendicular axis (*y* axis is assumed for illustrative purposes) to create variations in phase along that axis and yield one *ky* value in *k* space. This is followed by a frequency encoding gradient along a perpendicular axis (*x* axis is assumed for illustrative purposes). The frequency encoding gradient is turned on simultaneously with MR signal acquisition and is thus often denoted the 'readout gradient'. Since the readout gradient ensures varying frequencies at different spatial locations, a unique *kx* value is recorded in *k* space for each data point. After each readout, the phase encoding gradient amplitude is changed to generate another *ky* value and the same readout gradient is applied again during MR signal acquisition. In this way, *k* space is traversed until enough spatial frequency values are acquired, at which point the magnetization value at each spatial location can be extrapolated via a Fourier transform.

3.2 Pulse Sequences

Variety in the form of MR images is achieved through manipulation of the magnetization and phase distribution of spins by subjecting them to a sequence of RF and gradient pulses. Such application of multiple RF and gradient pulses to create a particular type of MR image is called a 'pulse sequence' and lies at the heart of MR experiments. Pulse sequences are typically designed such that data acquisition coincides with an echo, where phase coherence is maximized, yielding a stronger signal. This section reviews the two fundamental echo types which serve as foundation for most MR pulse sequences: spin echoes and gradient echoes.

3.2.1 Spin Echo

In spin echo imaging, a 90° RF pulse is initially applied and has the effect of tipping over the magnetization from the longitudinal plane onto the transverse plane. Once the 90° RF pulse is turned off , the spins begin to dephase due to field inhomogeneities. At a certain time τ after the 90° RF pulse, a 180° RF pulse is applied and rotates the magnetization 180° in the transverse plane, negating the phases of the spins. The spins however keep dephasing after the 180° RF pulse is turned off such that at time 2τ the spins rephase, producing a strong signal called a 'spin echo' [8].

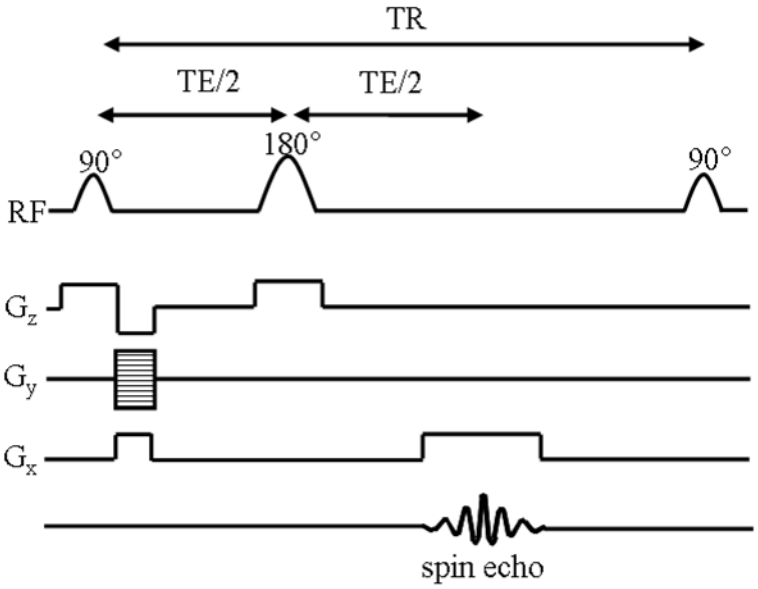

Figure 3.2 Spin echo pulse timing diagram. A slice selection gradient pulse is turned on along the *z* axis (G_z) while the 90° RF pulse is applied, phase encoding gradient pulses are turned on along the *y* axis (G_y) and a frequency encoding gradient pulse or readout gradient pulse is turned on along the *x* axis such that the data collection window is centered over the spin echo. Diagram reproduced from [8].

The echo time (TE) is the time between the initial 90° RF pulse and echo formation and is an important pulse sequence parameter for developing contrast in MR images. The repetition time (TR) is the time between successive 90° RF pulses and is equally important in determining contrast in MR images. The amplitude of the spin echo signal is given by

$$A_{SE} = M_{xy}(1 - e^{-\frac{TR}{T_1}})e^{-\frac{TE}{T_2}} \tag{3.13}$$

3.2.2 Gradient Echo

As the name implies, gradient echo imaging makes use of gradient pulses versus RF pulses to create an echo. In gradient echo imaging, after the initial RF pulse—which need not be a 90° RF pulse—is applied, a gradient pulse is applied in the transverse plane for half of the echo time (TE/2). This has the effect of causing the spins to start dephasing. At time TE/2, the polarity of the gradient pulse is reversed and has the effect of causing the spins to start negating their acquired phases. The reversed polarized gradient pulse is left on for time TE/2 at the end of which (at time TE) there is a strong signal called a ‘gradient echo’ [8].

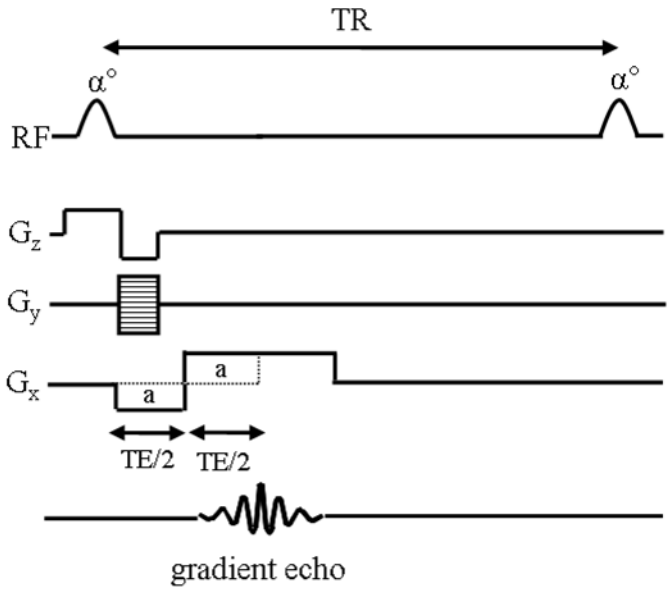

Figure 3.3 Gradient echo pulse sequence timing diagram. A slice selection gradient pulse is played out on the *z* axis (G_z) while the α ° RF pulse is applied, phase encoding gradient pulses are played out on the *y* axis (G_y) and a frequency encoding gradient pulse or readout gradient pulse is played out on the *x* axis such that the data collection window is centered over the spin echo. Diagram reproduced from [8].

The amplitude of the gradient echo signal is given by

$$A_{GE} = M_{xy}(1-e^{-\frac{TR}{T_1}})\frac{\sin(\alpha)e^{-\frac{TE}{T_2}}}{1-\cos(\alpha)e^{-\frac{TR}{T_1}}} \tag{3.14}$$

3.3 Diffusion

Robert Brown is generally credited with first observing diffusion as the seemingly random motion of pollen grains suspended in water, during the summer of 1827 [9]. Now understood to be the result of kinetic energy being transferred from randomly moving water molecules to the pollen grains, such motion is eponymously termed Brownian motion.

Adolf Fick subsequently advanced mathematical formalism to describe the diffusive flow (flux) of particles along a concentration gradient [10]. Fick's first law of diffusion relates the flux to the concentration gradient and postulates that the flux goes from regions of high concentration to regions of low concentration with a magnitude that is proportional to the concentration gradient

$$J = -D\frac{\partial \phi}{\partial x} \tag{3.15}$$

where *J* is the diffusive flux, *D* is the diffusion coefficient or diffusivity, ϕ is the concentration gradient and *x* is the position.

Fick's second law of diffusion follows from the first and draws on conservation of mass to describe how the concentration gradient changes over time due to diffusion

$$\frac{\partial \phi}{\partial t} = D\frac{\partial^2 \phi}{\partial x^2} \tag{3.16}$$

where *t* is time.

Albert Einstein advanced this work, demonstrating that the diffusion coefficient is related to the gas constant *R*, absolute temperature *T*, Avogadro's number N_A, viscosity η and the radius of molecules *r* [11]

$$D = \frac{RT}{N_A 6\pi\eta r} = \frac{kT}{6\pi\eta r} \tag{3.17}$$

where *k* is the Boltzmann constant, $\frac{R}{N_A}$. In an unrestricted medium, the motion of individual molecules is thus dictated by thermodynamics and the probability of collision with fellow molecules. Resolving the diffusion equations, it is possible to chart the probabilistic path of a typical molecule: the probability that a molecule at position $\boldsymbol{r_0}$ will end up at position $\boldsymbol{r}$ after a certain time *t* is given by

$$P(\boldsymbol{r} \mid \boldsymbol{r}_0, t) = \frac{1}{(4\pi Dt)^{\frac{3}{2}}} e^{-\frac{(\boldsymbol{r}-\boldsymbol{r}_0)^2}{4Dt}} \tag{3.18}$$

and the mean displacement, λ_r is expressed as

$$\lambda_r = \sqrt{6Dt} \tag{3.19}$$

The pollens in Robert Brown's initial experiment and Albert Einstein's diffusion coefficient represent diffusion of unrestricted molecules. However, diffusion in biologic tissue is often subject to endemic barriers. Hence, diffusion in biologic tissues is described more accurately by an effective or apparent diffusion coefficient (*ADC*), accounting for indigenous tissue properties.

3.4 Diffusion Weighted MRI

Diffusion is most commonly measured in MRI by introducing a pair of diffusion sensitizing gradients to a spin echo MRI pulse sequence. The first diffusion gradient (amplitude *G*, duration δ) serves to dephase the protons. Following this, some time (Δ) is allowed for protons to diffuse, after which a second diffusion gradient identical to the first, is applied with the intention of rephasing the protons.

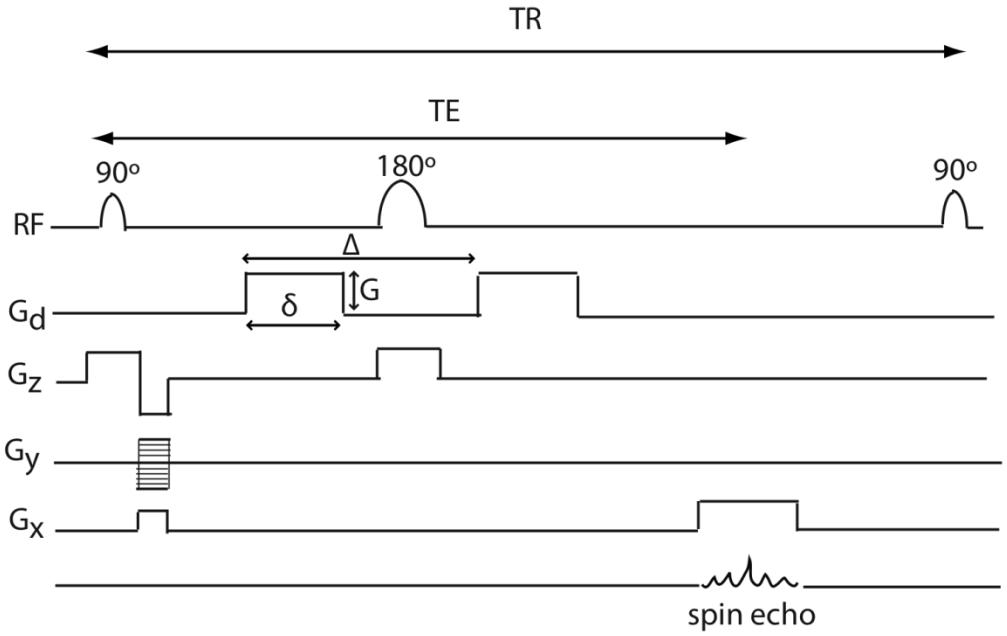

Figure 3.4 Diffusion weighted spin echo pulse sequence timing diagram. Diffusion sensitizing gradients pulses are turned on along sets of orthogonal directions (G_d). The amplitude of the diffusion gradient pulse is expressed as G, the duration as δ and the time between both pulses as Δ. A slice selection gradient pulse is turned on along the *z* axis (G_z) while the 90° RF pulse is applied, phase encoding gradient pulses are turned on along the *y* axis (G_y) and a frequency encoding gradient pulse or readout gradient pulse is turned on along the *x* axis such that the data collection window is centered over the spin echo.

If the protons have not moved in between the pair of diffusion gradients, their magnetizations are exactly refocused by the second gradient pulse and there is no signal attenuation at echo time. However, if the protons have diffused in between the pair of gradient pulses, their magnetizations do not refocus coherently, leading to a net spin echo signal attenuation which is proportional to the strength of the diffusion gradient. The relationship between the amount of echo signal attenuation and proton motion is given by

$$\frac{S_i}{S_0} = e^{-b_i D} \tag{3.20}$$

where S_0 is the signal measured with the diffusion sensitizing gradients turned off (i.e. $b = 0$), S_i is the signal measured with the motion sensitizing gradient pulses turned on to some b_i and D is the diffusion coefficient typically expressed in square millimeters per second $\left(\frac{mm^2}{s}\right)$. The 'b factor' ($b_i$) has inverse units to the diffusion coefficient $\left(\frac{s}{mm^2}\right)$, represents the overall sensitivity of the pulse sequence to motion or the degree to which the measured signal is diffusion weighted, and is given by the equation [12]

$$b_i = \gamma^2 G^2 \delta^2 \left(\Delta - \frac{\delta}{3} \right) \tag{3.21}$$

3.5 Diffusion Tensor MRI

In the absence of anisotropy, diffusion can be wholly described by the diffusion coefficient, a single scalar parameter. However, in the presence of anisotropy, a single scalar coefficient is no longer sufficient to fully characterize diffusion. A tensor, $\underline{\boldsymbol{D}}$, which fully describes motion along each direction and correlation between these directions is required [13]

$$\underline{\boldsymbol{D}} = \begin{pmatrix} D_{xx} & D_{xy} & D_{xz} \\ D_{yx} & D_{yy} & D_{yz} \\ D_{zx} & D_{zy} & D_{zz} \end{pmatrix} \tag{3.22}$$

The tensor is symmetric such that $D_{ij} = D_{ji}$, where $i, j = x, y, z$. In a reference frame [x', y', z'] which coincides with the principal directions of diffusivity, off diagonal terms in the tensor are null and the tensor is reduced to its diagonal components, $D_{xx'}$, $D_{yy'}$, $D_{zz'}$. The echo attenuation becomes

$$\frac{S_i}{S_0} = e^{-\left(b_{x'x'} D_{x'x'} + b_{y'y'} D_{y'y'} + b_{z'z'} D_{z'z'} \right)} \tag{3.23}$$

In practice however, measurements are made in the reference frame [x, y, z] of the MRI scanner gradients which rarely coincide with the principal directions of diffusivity. Thus, it becomes necessary to consider the coupling of non-diagonal tensor terms, D_{ij} ($i \neq j$), and the echo attenuation becomes

$$\frac{S_i}{S_0} = e^{-\left(\sum_{i=x,y,z} \sum_{j=x,y,z} b_{ij} D_{ij} \right)} \tag{3.24}$$

3.5.1 Diffusion Tensor Parameters

The diffusion tensor can be analyzed to provide information on the principal direction of diffusion, the mean diffusivity and the degree of anisotropy in each volume element (voxel) [13]. The three principal components of the diffusion tensor (the eigenvectors) and their corresponding diffusivities (the eigenvalues) can be determined by diagonalizing [14, 15] the diffusion tensor. Diagonalization amounts to determining the reference frame [x', y', z'] where the off diagonal terms in the diffusion tensor are null:

$$\boldsymbol{\Lambda} = \boldsymbol{R} \cdot \underline{\boldsymbol{D}} \cdot \boldsymbol{R}^T \tag{3.25}$$

where $\boldsymbol{\Lambda} = \begin{pmatrix} \lambda_1 & 0 & 0 \\ 0 & \lambda_2 & 0 \\ 0 & 0 & \lambda_3 \end{pmatrix}$ is the diagonalized matrix

and $\boldsymbol{R} = \begin{pmatrix} \varepsilon_{1x} & \varepsilon_{2x} & \varepsilon_{3x} \\ \varepsilon_{1y} & \varepsilon_{2y} & \varepsilon_{3y} \\ \varepsilon_{1z} & \varepsilon_{2z} & \varepsilon_{3z} \end{pmatrix}$ is the rotation matrix used to diagonalize $\boldsymbol{D}$

Diagonal terms in Λ represent the eigenvalues $(\lambda_1 > \lambda_2 > \lambda_3)$ and the columns of $\boldsymbol{R}$ are comprised of the corresponding eigenvectors. Eigenvalues and eigenvectors are rotationally invariant, meaning their values are independent of the MRI coordinate system. As such, standardized scalar parameters can be derived as functions of the eigenvalues and eigenvectors.

One such parameter is the mean diffusivity or *ADC*, which is equivalent to one-thirds the trace of the diffusion tensor or the average of the eigenvalues:

$$ADC = \frac{Tr(\underline{\boldsymbol{D}})}{3} = \frac{D_{xx} + D_{yy} + D_{zz}}{3} = \frac{\lambda_1 + \lambda_2 + \lambda_3}{3} \tag{3.26}$$

The degree of anisotropy is captured in the relative anisotropy (*RA*) and fractional anisotropy (*FA*). The RA represents the ratio of the anisotropic part of $\underline{\boldsymbol{D}}$ to the isotropic part of $\underline{\boldsymbol{D}}$ [13]:

$$RA = \frac{\sqrt{(\lambda_1 - \lambda_2)^2 + (\lambda_2 - \lambda_3)^2 + (\lambda_3 - \lambda_1)^2}}{\lambda_1 + \lambda_2 + \lambda_3} \tag{3.27}$$

The FA describes the fraction of the magnitude of $\underline{\boldsymbol{D}}$ that is due to anisotropic diffusion [13]:

$$FA = \frac{\sqrt{(\lambda_1 - \lambda_2)^2 + (\lambda_2 - \lambda_3)^2 + (\lambda_3 - \lambda_1)^2}}{\sqrt{2}\sqrt{\lambda_1^2 + \lambda_2^2 + \lambda_3^2}} \tag{3.28}$$

3.6 Contrast Enhanced MRI

The use of contrast agents in MRI has emerged as a non-invasive tool for cancer detection, diagnosis, staging, and assessment of treatment response. Dynamic contrast enhanced MRI (DCE-MRI) is sensitive to differences in blood volume and vascular permeability, characteristics associated with tumor angiogenesis, and is thus useful for characterizing tumor response to anti-angiogenic treatment [16, 17]. Tumor microvascular measurements by DCE-MRI have been found to correlate with prognostic factors (such as tumor grade, microvessel density [MVD], and vascular endothelial growth factor [VEGF] expression) and with recurrence and survival outcomes [18].

Contrast in unenhanced MRI comes from exploiting the intrinsic variation in proton relaxation times and proton density, evident in different tissues. With contrast enhanced MRI, paramagnetic contrast agents—such as Gadolinium containing compounds—can be used to further alter tissue proton relaxation rates. DCE-MRI is performed by obtaining sequential MR images before, during, and after the injection of a contrast agent. T_2* or susceptibility-weighted MRI can be used to provide information about the perfusion of the contrast agent by estimating the transient first-pass effects of contrast agent injection. The T_2* effect is measured as a rapid decrease and subsequent recovery of signal intensity after bolus injection. However this requires a rapid imaging method and tissue coverage is often sacrificed for high temporal resolution.

Dynamic T_1-weighted imaging is an alternative to T_2* weighted imaging and can be used over a longer time course to observe the extravasation of contrast agent from the vascular space to the interstitial space, providing information about blood volume and microvascular permeability. The accumulation of contrast agent in the interstitium results in a signal increase on T_1-weighted MR images. A subsequent wash-out effect can be observed if the vascular permeability is high and there is reflux of contrast agent to the vascular space. Signal intensity is proportional to the contrast agent concentration in affected voxels. Fitting such DCE MRI data to an appropriate pharmacokinetic model, it is possible to derive estimates of parameters related to blood volume and permeability that are hallmarks of the angiogenic phenotype associated with most cancers [18].

3.7 Tracer Pharmacokinetics

The principles of tracer pharmacokinetics can be applied to DCE-MRI with some considerations, if the relationship between signal intensity and contrast agent concentration is understood. Pioneering work towards understanding this relationship is generally credited to Tofts et al [19, 20]. It is necessary to know the intrinsic tissue T_1 (pre-contrast) to accurately relate any changes in signal intensity to the concentration of contrast agent in the tissue, C_t. The tissue contrast as a function of time $C_t(t)$ depends on arterial blood plasma concentration $C_p(t)$, which itself depends on cardiac output and the mode of injection (short versus long bolus). The $C_p(t)$ or arterial input function (AIF) is generally measured by including a large vessel in the imaging field of view. Variability in $C_p(t)$ can have a significant effect on derived pharmacokinetic parameters. $C_t(t)$ and $C_p(t)$ are related according to the generalized equation [21]:

$$\frac{dC_t}{dt} = K^{trans}(C_p - \frac{C_t}{\upsilon_e}) = K^{trans}C_p - \kappa_{ep}C_t \tag{3.29}$$

where K^{trans} is the forward flow volume transfer constant between the blood plasma and extravascular extracellular space (EES) per unit volume of tissue (min^{-1}), κ_{ep} is the back flow rate constant between the EES and blood plasma (min^{-1}), and υ_e is the volume of the extravascular extracellular space per unit volume of tissue. Note that the forward flow transfer constant is alternatively denoted as K^{ps}. The solution to Equation 3.29 can be expressed as [22]:

$$C_t(t) = (1 - fPV) \cdot K^{PS} e^{-k_{ep}t} \otimes C_p(t) + fPV \cdot C_p(t) \tag{3.30}$$

where fPV is the fractional plasma volume, and is unitless, similar to υ_e.

While the application of tracer kinetics to MRI depend on measurements of the intrinsic tissue T_1 value and an AIF, limitations in clinical practice sometimes make these measurements infeasible. An assumption of linearity between signal intensity and contrast concentration can be made (eliminating the need for pre-contrast T_1), or the signal intensity time curve can be quantified using empirical quantitative measures such as the initial area under the curve, peak enhancement, time to peak enhancement, or signal enhancement ratio (SER) [18]. It is also possible to use published estimates from healthy controls in lieu of AIF measurements.

3.8 Signal Enhancement Ratio

As hinted earlier, there are multiple approaches to quantifying DCE-MRI data. The signal enhancement ratio is one such approach that enjoys clinical practicality. This approach relies on sampling the contrast uptake curve at three time points to characterize both initial enhancement and washout in lesions. The percentage of enhancement (PE) after the injection of contrast material represents uptake and is given by [23]:

$$PE = \frac{S_1 - S_0}{S_0} \times 100\% \tag{3.31}$$

where S_0 is the pre-contrast time point and S_1 is the early post-contrast time point. The signal enhancement ratio (SER) compares early to late enhancement in the lesions to identify washout and is defined as [23]:

$$SER = \frac{S_1 - S_0}{S_2 - S_0} \tag{3.32}$$

where S_2 is the late post-contrast time point.

3.9 References

1. Obituary, *Paul Lauterbur, father of MRI*, in *Economist*. 2007: London. p. 84-84.
2. Berman, J.I., *Localization and Assessment of Subcortical White Matter Pathways with Diffusion Tensor Magnetic Resonance Imaging*, in *Bioengineering*. 2005, University of California San Francisco and University of California Berkeley: San Francisco.
3. Chow, T.L., *Electromagnetic Theory*. 2006, Sudbury, MA: Jones and Bartlett.
4. Bracewell, R.N., *The Fourier Transform and Its Applications*. 3rd ed. 2000, Boston: McGraw-Hill.
5. Haacke, E.M., et al., *Magnetic Resonance Imaging: Physical Principles and Sequence Design*. 1999, New York: Wiley-Liss.
6. Buxton, R.B., *Introduction to Functional Magnetic Resonance Imaging: Principles and Techniques*. 2002, Cambridge: Cambridge University Press.
7. Nishimura, D.G., *Principles of Magnetic Resonance Imaging*. 1996: Stanford.
8. Ozturk, E.I., *Implementation of Parallel Imaging Techniques for Lipid Unaliasing and Faster Acquisition for Improving Spatial Characterization Magnetic Resonance Spectroscopic Imaging of Gliomas*, in *Bioengineering*. 2007, University of California San Francisco and University of California Berkeley: San Francisco.
9. Brown, R., *A brief account of microscopical observations made in the months of June, July and August, 1827, on the particles contained in the pollen of plants; and on the general existence of active molecules in organic and inorganic bodies.*, in *Phil. Mag.* 1857. p. 161-173.
10. Fick, A., *On liquid diffusion*, in *Phil. Mag.* 1855. p. 30-39.
11. Einstein, A., *On the Motion—Required by the Molecular Kinetic Theory of Heat—of Small Particles Suspended in a Stationary Liquid.* Ann Phys, 1905. **19**: p. 549-560.
12. Neil, J.J., *Measurement of Water Motion (Apparent Diffusion) in Biological Systems.* Concepts Magn Reson, 1997. **9**(6): p. 385-401.
13. Le Bihan, D., et al., *Diffusion tensor imaging: Concepts and applications.* J Magn Reson Imaging, 2001. **13**(4): p. 534-546.
14. Basser, P.J., J. Mattiello, and D. Le Bihan, *MR diffusion tensor spectroscopy and imaging.* Biophys J, 1994. **66**(1): p. 259-267.
15. Basser, P.J., J. Mattiello, and D. Le Bihan, *Estimation of the effective self-diffusion tensor from the NMR spin echo* J Magn Reson Imaging, 1994. **103**(3): p. 247-254.
16. Miller, J.C., et al., *Imaging Angiogenesis: Applications and Potential for Drug Development* J Natl Cancer Inst, 2005. **97**(3): p. 172-187.
17. Rehman, S. and G.C. Jayson, *Molecular Imaging of Antiangiogenic Agents* Oncologist, 2005. **10**(2): p. 92-103.
18. Hylton, N., *Dynamic Contrast-Enhanced Magnetic Resonance Imaging As an Imaging Biomarker* J Clin Oncol, 2006. **24**(20): p. 3293-3298.
19. Tofts, P.S. and A.G. Kermode, *Measurement of the blood-brain barrier permeability and leakage space using dynamic MR imaging. 1. Fundamental concepts.* Magn Reson Med, 1991. **17**(2): p. 357-367.
20. Tofts, P., *Modeling tracer kinetics in dynamic Gd-DTPA MR imaging.* J Magn Reson, 1997. **7**(1): p. 91-101.

21. Tofts, P., et al., *Estimating kinetic parameters from dynamic contrast-enhanced T(1)-weighted MRI of a diffusable tracer: standardized quantities and symbols.* J Magn Reson, 1999. **10**(3): p. 223-232.
22. Langen, A.J.d., et al., *Use of H215O-PET and DCE-MRI to Measure Tumor Blood Flow.* Cancer Imaging, 2007. **13**(6): p. 631-644.
23. Partridge, S., et al., *Accuracy of MR imaging for revealing residual breast cancer in patients who have undergone neoadjuvant chemotherapy.* Am J Roentgenol, 2002. **179**(5): p. 1193-1199.

Chapter 4

Investigating the Added Value of Diffusion Weighted MRI for Treatment Monitoring in a Breast Tumor Xenograft Model[1]

This chapter describes the results of a pre-clinical study investigating whether quantitative MRI parameters are sensitive to the effects of targeted therapy. The ability of diffusion weighted MRI, specifically the ADC, to add value to more traditional MRI parameters, in the context of treatment monitoring is explored.

4.1 Background

A promising approach to improving anti-tumor efficacy in cancer treatment involves the combination of targeted agents aimed at inhibiting signal transduction in tumors, with cytotoxic drugs. An advantage to this approach is that signaling pathways and associated receptors implicated in different cancer types can be specifically targeted. The human growth factor receptor (HER) family of tyrosine kinases (TKs) plays an important role in cell differentiation, proliferation, migration and survival [1]. HER TKs have been implicated in breast cancer [2] and mediate some of the angiogenic properties of cancer cells [3, 4]. Dysregulation of HER TKs has been shown to promote the development and growth of cancer [1]. This makes HER TKs an attractive target for the design of anti-tumor targeting agents.

Gefitinib (Iressa^{TM}), an HER family tyrosine kinase inhibitor (TKI), has demonstrated anti-tumor activity in HER family over-expressing breast tumor cells *in vitro* and *in vivo* [5, 6]. Pre-clinical studies have shown enhanced efficacy from the combined administration of gefitinib with chemotherapy [7, 8]. However, this effect was moderate and recent evidence suggests that the ability of gefitinib to suppress survival signaling might be transient, requiring much higher doses to effectively suppress HER family survival signaling [9]. High daily doses of HER TKIs are impractical due to their dose-limiting toxicities. However, when used as chemo-sensitizers, HER TKIs can be administered for short periods in much higher doses immediately prior to chemotherapy and can potentially serve to prime tumor microenvironments for better delivery of chemotherapeutic agents. Optimal priming of the tumor microenvironment will likely depend on

[1] This Chapter is adapted from an article published in *Journal of Magnetic Resonance Imaging* (Aliu et al., 2009)

precise timing of HER TKI administration relative to chemotherapy. Measurement methods that are sensitive to the effects of HER TKIs and can be used for *in vivo* monitoring are needed.

MRI methods have been used to detect changes induced by other targeting agents, notably those directed towards the vascular endothelial growth factor (VEGF) [10], but few studies have applied MRI to study the effects of HER family targeting agents. The present study assessed the ability of multiple MRI parameters, tumor volume, ADC, transendothelial permeability (K^{ps}) and fractional plasma volume (fPV), to detect gefitinib induced changes in a breast tumor xenograft model.

The ADC, obtained from diffusion-weighted MRI, is a noninvasive imaging technique that measures the mobility of water in tissues. Diffusion in MRI is generally observed through the introduction of a pair of bipolar motion sensitizing gradient pulses [11]. Studies have shown that the ADC is inversely correlated with tissue cellularity [12, 13], reflecting greater restriction to motion in denser tissue. In recent years, the ADC has emerged as a potential surrogate indicator of tumor response to therapy [14-16] and has been used to differentiate malignant tumors from benign lesions and normal tissue [17-20].

DCE-MRI is a technique for evaluating the physiology of microcirculation. It entails serial acquisition of MR images before, during and after intravenous injection of contrast media into tissues of interest. By fitting DCE-MRI data acquired using macromolecular contrast media such as albumin-$(GdDTPA)_{30}$ to an appropriate pharmacokinetic model, it is possible to extract quantitative physiologic parameters that describe microvascular wall permeability (K^{ps}) and the fractional plasma volume (fPV). Numerous studies have used DCE-MRI to assess vascular changes associated with response to anti-angiogenic therapy [21-24]. Several studies have demonstrated decreased K^{ps} in response to effective anti-angiogenic therapy, which is generally attributed to less leaky vessels. The fPV has also been used as a surrogate marker of tumor angiogenesis.

The aims of the present study were to evaluate the ability of MRI parameters to detect the effects of gefitinib administered as a potential means of improving chemotherapy administration and to evaluate whether MRI parameters can differentiate between two different gefitinib dose treatment regimens.

4.2 Methods

4.2.1 Tumor Model

Immune deficient female mice (*Nu/nu*; age 7-8 weeks; Taconic, Germantown, New York, USA) were implanted subcutaneously with 17β estradiol pellets (0.72 mg/pellet; Innovative Research, Sarasota, Florida, USA) 24-48 hours prior to tumor cell injection. Human BT474, HER2-neu over-expressing breast cancer cells optimized for growth *in vivo*, were implanted subcutaneously into the axillary flank (1×10^7 cells/injection). Tumors were allowed to grow to approximately 200-400 mm^3 (typically two weeks after cell injection) prior to imaging or treatment. All animal

usage was approved by the institutional animal care committee at the University of California in Berkeley and San Francisco.

4.2.2 In-vivo MRI Studies

Natural History

To establish the natural history of MRI parameters during the growth of BT474 tumors, a cohort of untreated mice (n=8) were imaged beginning two weeks after tumor cell injection, at approximately two day intervals over a two week period: baseline, day 2, day 4, day 7, day 9, day 11 and day 14. Diffusion-, T_1- and T_2- weighted images were acquired at each time point in all mice.

Gefitinib Treatment Study

For the treatment study, tumor bearing mice were treated with gefitinib according to three arms: daily dose (n=6); pulsed dose (n=6) and controls (n=5). In the daily treatment arm, mice were treated daily with gefitinib at the maximum tolerated daily dose of 150 mg/kg administered orally for 10 days. In the pulsed treatment arm, mice were treated for two days (day 2 and day 3) with gefitinib at the maximum tolerated dose of 1000 mg/kg administered orally. Control mice were treated daily with vehicle carrier for 10 days. All treatments were administered by oral gavage and mice in all three arms were imaged at baseline, day 4, and day 9. In addition to diffusion-, T_1- and T_2- weighted images, DCE images were acquired at each time point.

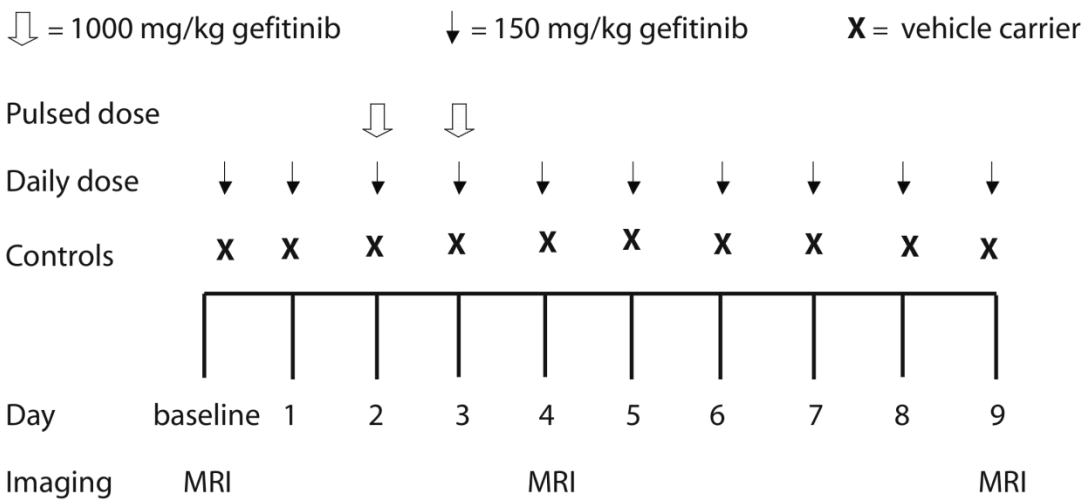

Figure 4.1 Mice in the gefitinib treatment study were treated according to three arms: daily dose (n=6); pulsed dose (n=6) and controls (n=5). Mice in the daily dose treatment arm received gefitinib daily at the maximum tolerated daily dose of 150 mg/kg for 10 days. Mice in the pulsed dose treatment arm received two doses (day 2 and 3) of gefitinib at the maximum tolerated dose of 1000 mg/kg. Control mice were treated daily with vehicle carrier for 10 days. All mice were imaged at baseline, day 4 and day 9.

4.2.3 MR Imaging

MR imaging was performed on a whole body 1.5 T GE Signa scanner (GE Healthcare, Milwaukee, Wisconsin, USA) using a wrist coil (Medical Advances, Milwaukee, Wisconsin, USA) and customized animal holder. Mice were imaged in pairs and were anesthetized by inhalation with 1.5% isoflurane administered via an MR-compatible mobile inhalation anesthesia system (Vet Equip, Pleasanton, California, USA). A 3D fast gradient recalled echo (FGRE) sequence was used to rapidly and reproducibly position mice.

Diffusion-weighted images were acquired using a diffusion sensitized single-shot fast spin echo sequence (TR = 9899 ms, effective TE = 69 ms, FOV = 100 × 100 mm, slice thickness = 3 mm, imaging matrix = 256 × 256). Ten axial diffusion-weighted slices centered around the tumor were acquired. Diffusion weighting was achieved with a gradient duration δ = 17.6 ms, gradient interval Δ = 22.8 ms, gradient strength G_D = 39.6 mT/m, and the *b*-value was calculated according to

$$b = \gamma^2 G_D^2 \delta^2 \left(\Delta - \frac{\delta}{3} \right) \qquad (4.1)$$

where γ is the gyromagnetic ratio of the proton. Weighting factors (*b*-values) of $b = 0$ and $b = 603$ s/mm^2 were applied.

T_1-weighted images were acquired using a variable flip angle 3D spoiled gradient echo sequence (TR = 27 ms, TE = 8 ms, flip angle = 40°, 20°, 8°, field of view (FOV) = 100 × 100 mm, slice thickness =1 mm, imaging matrix = 256 × 256 × 28).

T_2-weighted images were acquired using a fast spin echo sequence (TR = 5500 ms, TE = 81 ms, FOV = 100 × 100 mm, slice thickness = 1.5 mm, imaging matrix = 256 × 256).

Contrast-enhanced imaging was performed using a coronal T_1-weighted 3D FGRE sequence (TR = 9 ms, TE = 4ms, FOV = 100 ×100 mm, slice thickness = 1mm, imaging matrix = 256 × 256 × 28, acquisition time = 63 s). Axial images were acquired for tumor localization and five pre-contrast scans were acquired prior to injecting 0.03 mmol/kg albumin-$(GdDTPA)_{30}$ (Center for Pharmaceutical and Molecular Imaging at UCSF, San Francisco, California, USA) via the tail vein [25]. This was followed by 40 min of post-contrast imaging.

4.2.4 Image Analysis

MRI tumor volume was approximated on non-contrast enhanced 3D T_1-weighted images by manually delineating tumor boundary regions of interest (ROIs) sequentially on all tumor-appearing slices and summing the volumes. A single operator delineated all ROIs to ensure consistency. ADC maps were generated on a pixel-by-pixel basis from diffusion weighted images as described previously [26]. T_1 maps were generated from T_1-weighted images acquired at the three flip angles, 40°, 20° and 8°. A fitting routine implemented in IDL (version 6.1; Research Systems Inc., Boulder, Colorado, USA) was used to generate T_1 maps.

To interrogate potential effects of tumor necrosis on measurements, necrotic regions—typically presenting as hyper-intense regions on T_2-weighted images—were isolated using a semi-automated clustering technique [27, 28] implemented in MATLAB® (R2006a; The Mathworks Inc., Natick, Massachusetts, USA). Clusters were generated by considering T_2-weighted signal intensities in the entire tumor on a pixel-by-pixel basis and assigning pixels to clusters to minimize intra-cluster variance. Generated clusters were subsequently categorized as potentially necrotic based on visual inspection. Such potentially necrotic clusters were then classified as necrotic if pixel signal intensities were beyond three standard deviations from mean tumor T_2-weighted signal intensity. Five clusters were imposed to oversample the number of tumor components and empirically determined to provide the best compromise between maximizing tissue differentiation and minimizing computation time. Pixels on ADC maps corresponding to necrotic clusters on T_2-weighted images were excluded from ADC analysis.

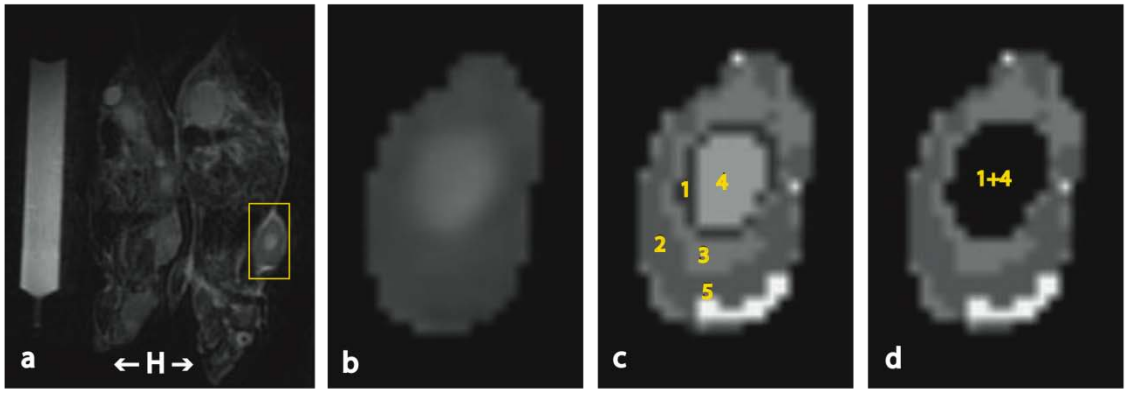

Figure 4.2 Tumor necrosis segmentation (a) Shows a representative T_2-weighted image of a pair of mice. Mice head (H) are indicated with arrows for orientation. Regions of interest (ROIs) were manually drawn around tumor margins on all tumor-appearing slices. The inset box demonstrates the extent of the tumor prior to ROI delineation. (b) Shows the tumor after isolation by ROI delineation. A region of central necrosis is evident. (c) Pixel intensities from within the isolated tumor and with the number of clusters to be imposed served as input to the clustering algorithm. The clustering algorithm assigned pixels to clusters to minimize intra-cluster variance and generated clusters numbered 1 through 5. (d) Generated clusters were visually inspected against the T_2-weighted image and categorized as potentially necrotic or not. Potentially necrotic clusters were then classified as truly necrotic if pixel intensities were beyond three standard deviations from mean tumor T_2-weighted intensity. Pixels belonging to necrotic clusters (clusters 1 and 4 in this case) were excluded from ADC analysis.

Quantitative analysis of T_1-weighted, albumin-$(GdDTPA)_{30}$ enhanced images was performed using a two-compartment unidirectional pharmacokinetic model incorporating pre-contrast tissue T_1 values to estimate K^{ps} and fPV from the relationship

$$C_t(t) = K^{ps} \int_0^t C_p(t')dt' + fPV \cdot C_p(t) \qquad (4.2)$$

where C_t and C_p are the concentrations of contrast media in tissue and plasma respectively as described previously [29-31]. Tumor boundaries were assigned manually in the DCE-MRI images. K^{ps} and fPV maps were estimated on a voxel-by-voxel basis for ROIs encompassing the whole tumor. Individual vascular input functions were determined from enhancing voxels in the abdominal aorta of each mouse and were assumed to decay mono-exponentially.

4.2.5 Statistics

A one-way repeated measures analysis of variance (ANOVA) design was used to establish significant differences over time in the natural history study. A two-way repeated measures ANOVA was used to establish differences in MRI parameters (mean tumor ADC, volume, K^{ps} and fPV) between the treatment groups (pulsed, daily, control) over time (baseline, day 4, day 9) in the gefitinib treatment study. Differences in cell density indices on H&E slides and apoptotic indices on caspase-3 slides, between the treatment groups, were established using a one-way ANOVA design. Tukey's Honestly Significant Difference test was used for post-hoc comparisons in all ANOVA designs. JMP (Version 6; SAS Inc., Cary, North Carolina, USA) was used for all statistics.

4.2.6 Histology and Immunohistochemistry

Mice in the gefitinib treatment study were euthanized immediately following imaging on day 9 and tumor tissues were harvested for histology and immunohistochemistry. Tumors were sectioned along the plane corresponding to DCE and diffusion-weighted image acquisition. Tumor tissues were processed, embedded in paraffin and sectioned at 5 μm thickness. Consecutive slices were stained with Hematoxylin and Eosin (H&E) to probe differences in cell density between groups and with rabbit anti-cleaved caspase-3 polyclonal antibody, 1:200 dilution (Cell Signaling Technology, Beverly, Massachusetts, USA) to assess potential apoptotic effects and any differences between groups. H&E tissue slides were analyzed on a Nikon microscope (Eclipse TE-2000E; Nikon, Tokyo, Japan). Two to three representative fields from non-necrotic regions were chosen from each slide. The microscope manufacturer's software (NIS-Elements AR 2.30) was used to generate a cell density index as the ratio of the area occupied by cells within a field to the total field area. Indices were then averaged for each of the three experimental groups in the gefitinib treatment study. Caspase-3 slides were analyzed on a Nikon microscope (Eclipse TS 100-F; Nikon, Tokyo, Japan). A 10 by 10 mm reticule (at magnification 40X) served as the field. An apoptotic index was computed as the ratio of apoptosis stained cells to the total number of cells in the field. This ratio was averaged across slides for each of the three experimental groups in the gefitinib treatment study.

4.3 Results

4.3.1 Natural History

MRI mean tumor volume increased exponentially ($144\,e^{0.25x}$ mm^3, $R^2 = 0.93$) over the course of the 14-day natural history study (*M*±*SEM*: 187±37, 202±29, 353±52, 370±52, 620±126, 561±99, 758±127 mm^3). There were significant differences ($F(6,47) = 6.27$, $p < .0001$) in mean tumor volume over time. Specifically, mean tumor volumes at day 9, day 11 and day 14 were significantly different from mean tumor volumes at baseline ($p < .050$). Mean tumor ADC remained relatively uniform over the course of the natural history study (*M*±*SEM*: 1151±28, 1041±66, 1121±59, 1020±74, 1155±70, 1078±56, 1090±55 mm^2/s). Mean tumor T_1 values stabilized after a slight decrease from baseline to day 2 (*M*±*SEM*: 1246±74, 1168±11, 1102±59, 1152±26, 1093±51, 1125±44, 1141±32).

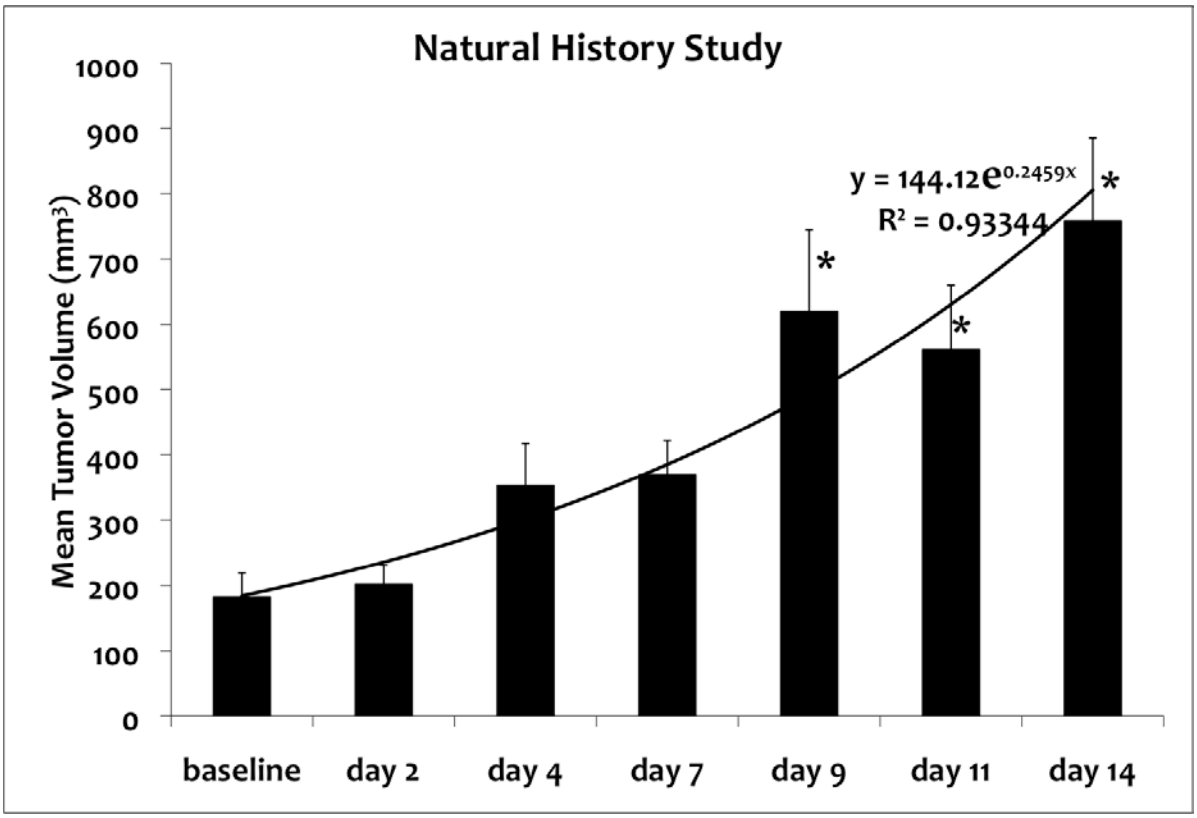

Figure 4.3 Mean tumor volumes in natural history study. Mean tumor volume increased exponentially in untreated mice over the course of 14 days. Tumor volumes at later time points (day 9, day 11, day 14) were significantly different from tumor volumes at baseline. Error bars denote standard error. Asterisks denote statistical difference from baseline.

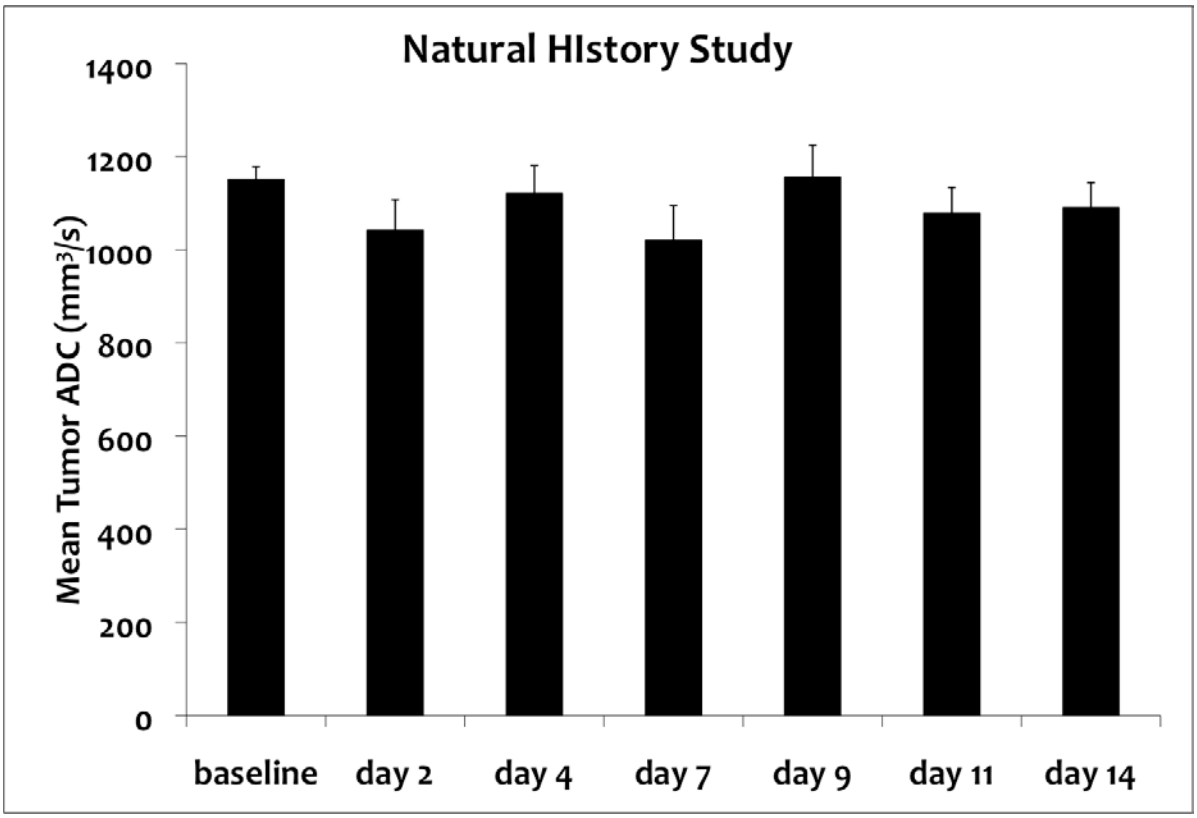

Figure 4.4 Mean tumor ADC values in natural history study. ADC values remained relatively uniform over the course of 14 days. Error bars denote standard error.

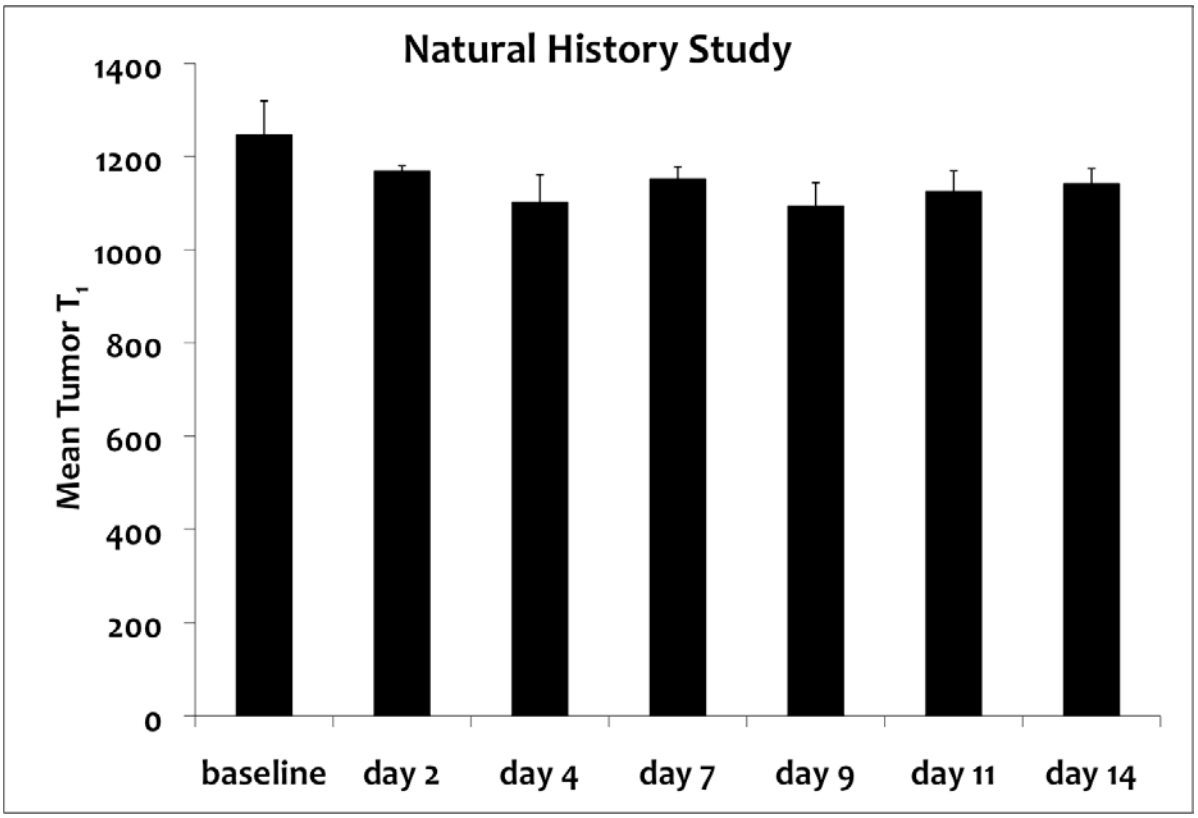

Figure 4.5 Mean tumor T_1 values in natural history study. T_1 values stabilized after a slight decrease from baseline to day 2. Error bars denote standard error.

4.3.2 Gefitinib Treatment Study

Trends in mean tumor volume, ADC and T_1, observed in the control group of the gefitinib treatment study were consistent with trends observed in untreated mice in the natural history study.

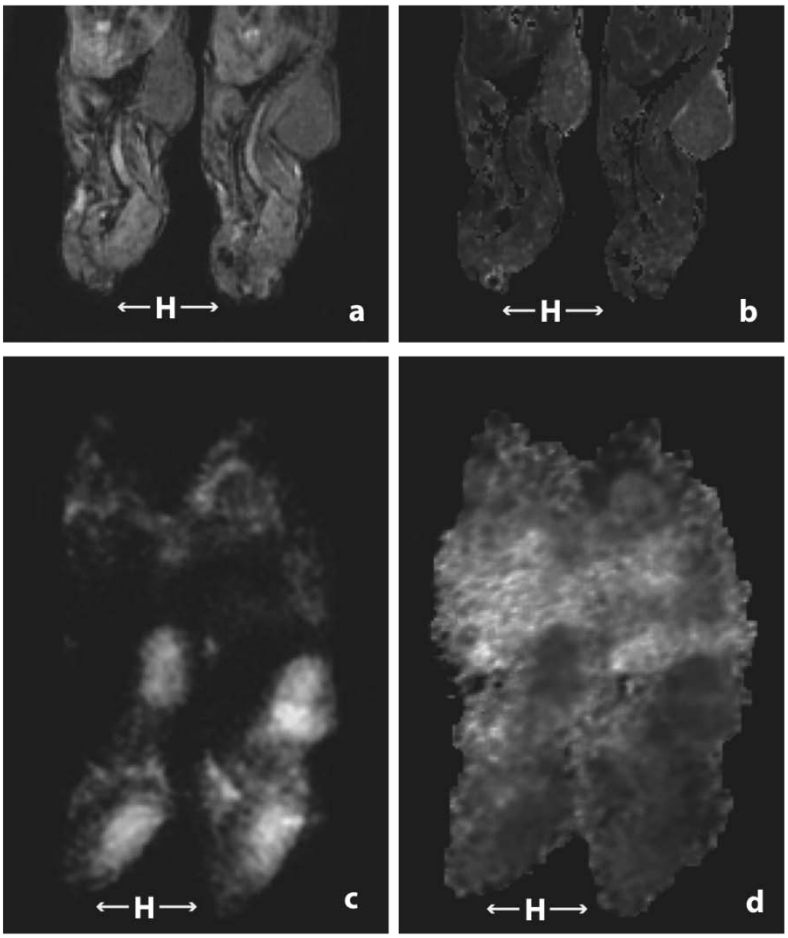

Figure 4.6 Representative MR images. (a) Shows a representative T_1-weighted image for a pair of mice acquired at flip angle 40°. Mice head (H) are indicated with arrows for orientation. (b) Shows the corresponding T_1 map generated from T_1-weighted images acquired at flip angles of 40°, 20° and 8°. (c) Shows a representative diffusion-weighted image (b-value = 603 s/mm^2). Mice head (H) are indicated with arrows for orientation. (d) Shows the corresponding ADC map.

Mean tumor volumes increased between baseline and day 9 in all three experimental groups but the two gefitinib treated groups increased at a slower rate relative to the control group. There was a significant main effect of treatment ($F(2,14.03) = 7.90$, $p = .0050$) and time ($F(2,19.56) = 34.69$, $p < .0001$) on mean tumor volumes. There was also an interaction effect of treatment and time ($F(4,18.92) = 8.22$, $p = .0005$). Post-hoc comparisons revealed that mean tumor volumes in all groups were not significantly different at baseline (*M*±*SEM*; pulsed: 361±25; daily: 244±22; control: 288±30 mm^3, $p > .050$) but both gefitinib treated groups were significantly different from the control group at day 9 (*M*±*SEM*; pulsed: 439±93; daily: 404±53; control: 891±174 mm^3, $p < .050$). There was a transient decrease in mean tumor volume observed in the pulsed dose group between baseline and day 4 but this trend was not statistically significant.

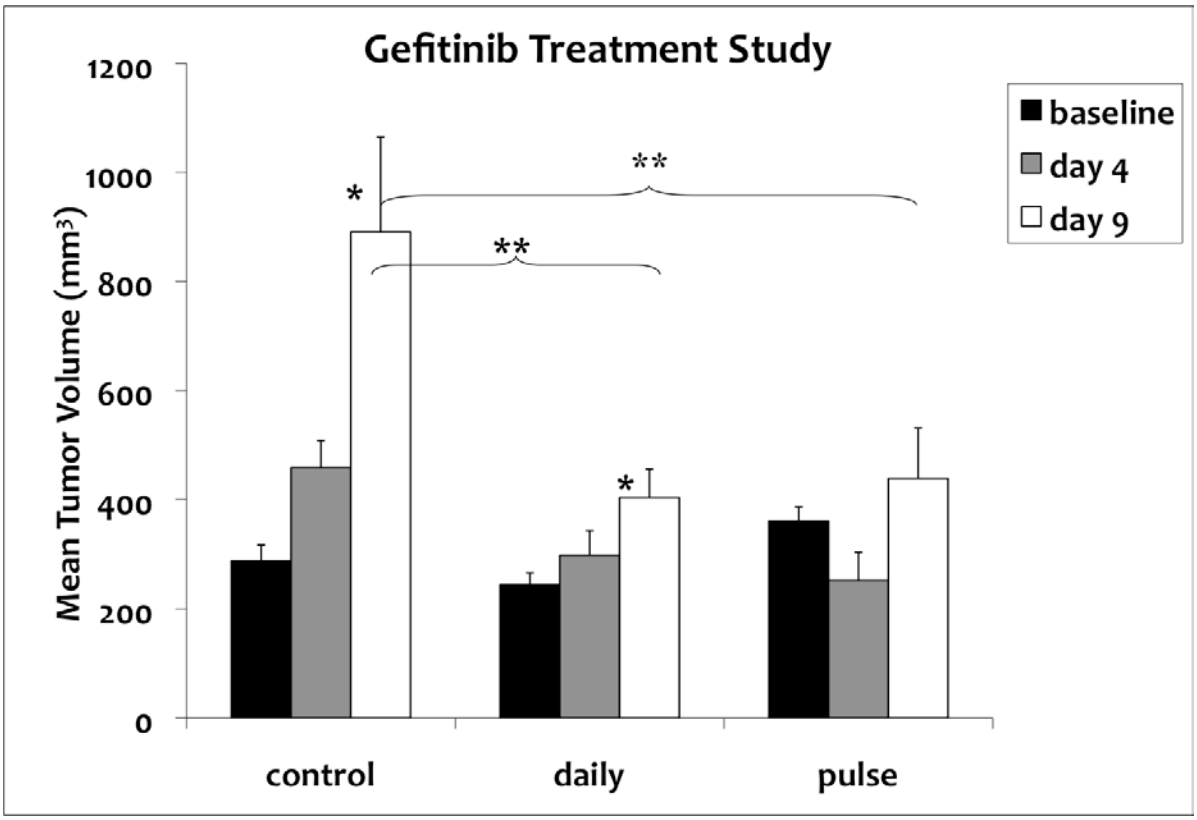

Figure 4.7 Mean tumor volume in gefitinib treatment study. Gefitinib treatment resulted in significant tumor growth inhibition; both gefitinib treated groups were statistically different from controls at day 9. A small reduction in tumor volume is observed with pulsed treatment at day 4. The gefitinib treated groups were not statistically different from each other. Error bars denote standard error, single asterisks denote statistical difference from baseline within groups, while double asterisks denote statistical difference between groups at time points conjoined with braces.

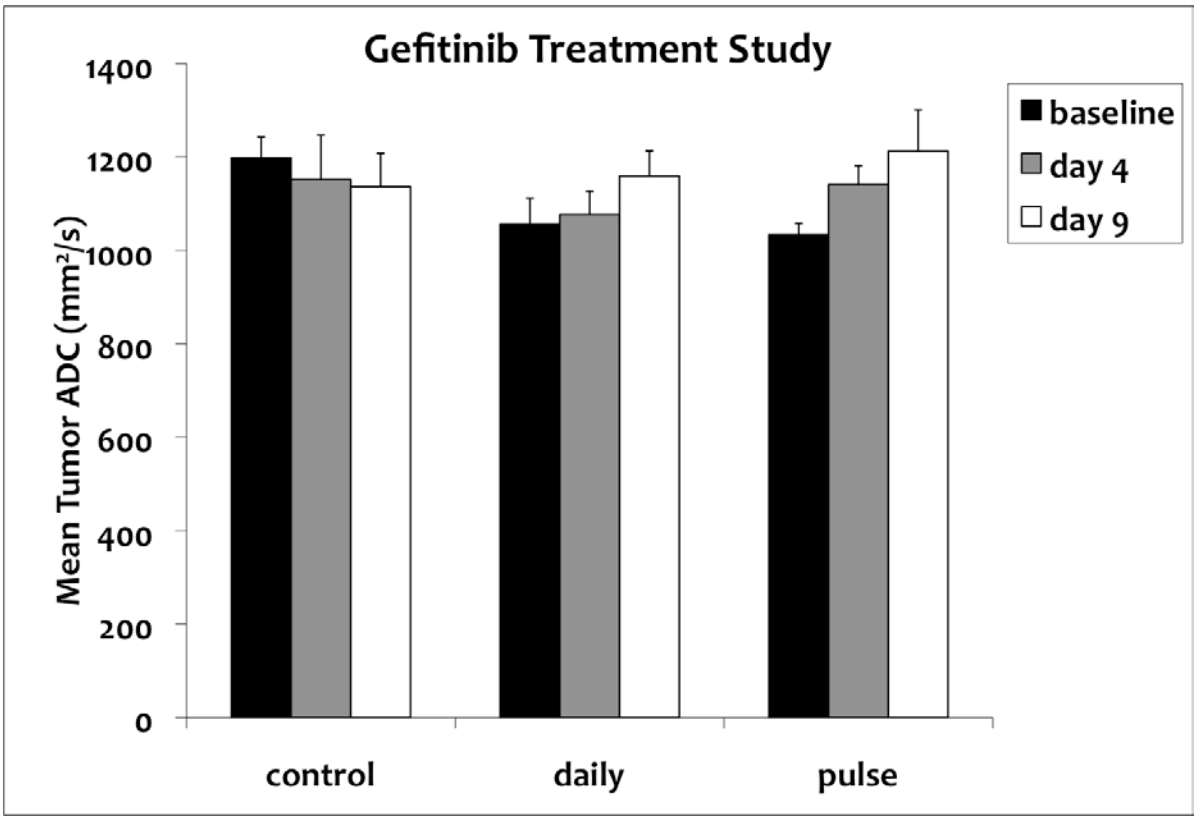

Figure 4.8 Mean tumor ADC in gefitinib treatment study. There was a trend of increasing ADC in both gefitinib treated groups while ADC in controls decrease slightly. Error bars denote standard error.

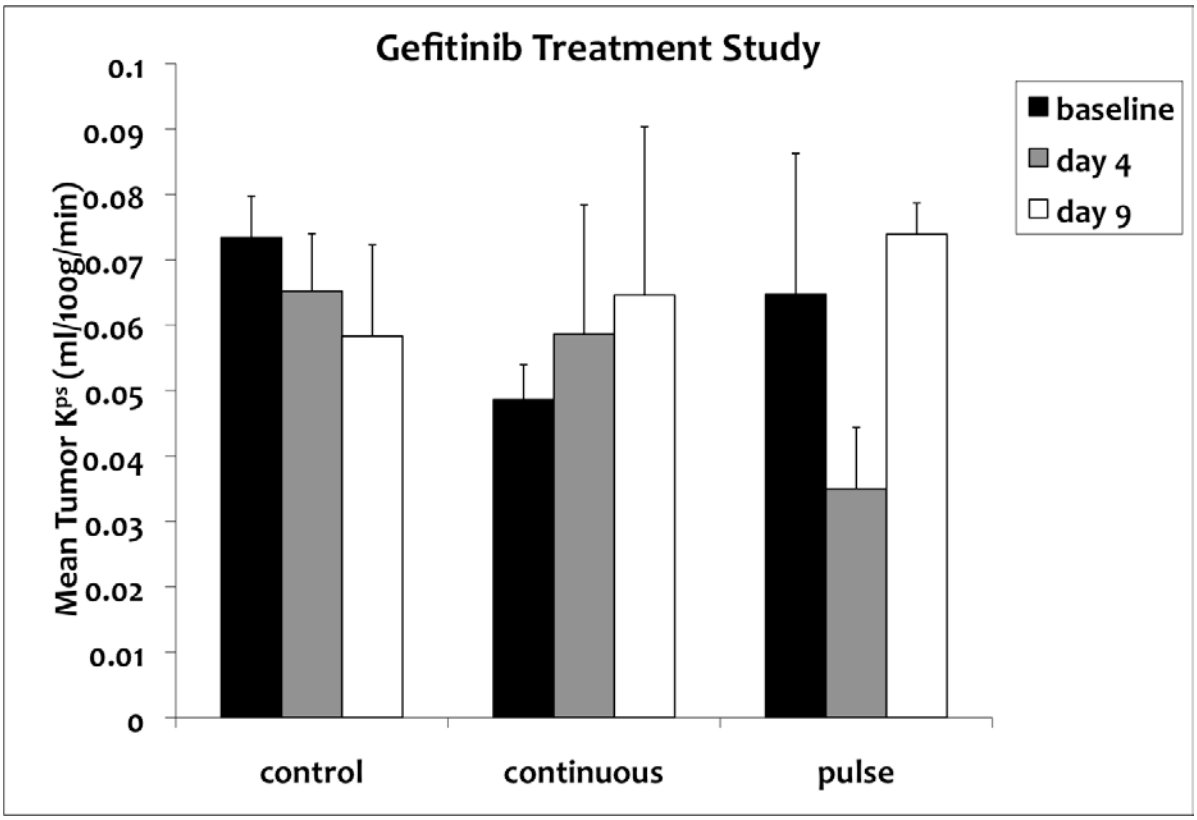

Figure 4.9 Mean tumor K^{ps} in gefitinib treatment study. K^{ps} decreased with pulsed treatment but rebounded afterwards and increased with daily treatment. Error bars denote standard error.

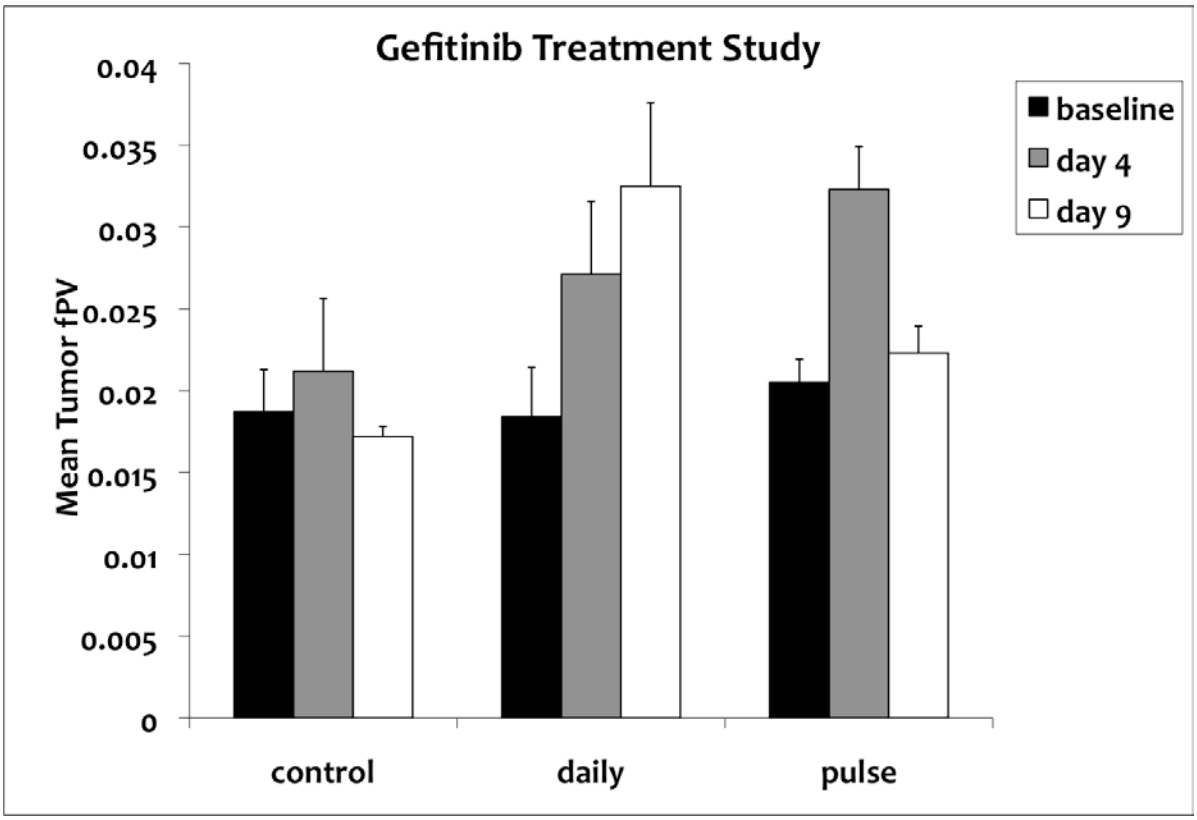

Figure 4.10 Mean tumor fPV in gefitinib treatment study. fPV increased in both gefitinib treated groups, decreasing afterwards with pulsed treatment. Error bars denote standard error.

As a general trend, mean tumor ADC increased in both gefitinib treated groups between baseline and day 9 (*M*±*SEM*; pulsed: 1034±24, 1141±40, 1212±89; daily:1056±56, 1077±50, 1159±53 mm^2/s) but remained relatively unchanged in the control group from baseline to day 9 (*M*±*SEM*; 1198±45, 1152±95, 1137±71 mm^2/s). However, there was no statistically significant effect of treatment or time on mean tumor ADC. Figure 4.8 displays mean tumor ADC trends in the gefitinib treatment study.

Mean tumor K^{ps} decreased from baseline to day 4 with a rebound at day 9 in the pulsed dose group (*M*±*SEM*; 0.0647±0.0215, 0.035±0.0094, 0.0739±0.0048 ml/100g/min), increased from baseline to day 9 in the daily dose group (*M*±*SEM*; 0.0486±0.0054, 0.0586±0.0198, 0.0646±0.0257 ml/100g/min) and decreased from baseline to day 9 in the control group (*M*±*SEM*; 0.0734±0.0064, 0.0652±0.0088, 0.0583±0.0140 ml/100g/min). However, there were no statistical differences between or within the groups. Figure 4.9 displays mean tumor K^{ps} trends.

Mean tumor fPV increased from baseline to day 4 before decreasing from day 4 to day 9 in the pulsed dose group (*M*±*SEM*; 0.0250±0.0014, 0.0323±0.0026, 0.0223±0.0016), increased from baseline to day 9 in the daily dose group (*M*±*SEM*; 0.0184±0.0030, 0.0271±0.0045, 0.0325±0.0051) and remained relatively uniform from baseline to day 9 in the control group (*M*±*SEM*; 0.0187±0.0026, 0.0212±0.0044, 0.0172±0.0006). There was a trend towards an effect

of treatment ($F(2,13.34) = 3.71$, $p = .0523$) and a significant main effect of time ($F(2,24.94) = 3.71$, $p = .0388$) but no statistically significant interaction between treatment and time, on mean tumor fPV. Figure 4.10 displays mean tumor fPV results.

Histological evaluation of tumors in the natural history study and in the gefitinib treatment study revealed noticeable central necrosis, and in some cases peripheral necrosis. There was a significant effect of treatment ($F(2,10) = 17.86$, $p < .0005$) on cell densities computed from H&E slides. Gefitinib treated groups were significantly less dense than the control group ($M \pm SEM$; pulsed: 0.15±0.01; daily: 0.17±0.01; control: 0.24±0.01, $p < .050$) but were not significantly different from each other. Qualitatively, the gefitinib treated groups were also observed to exhibit greater inter-nuclear spacing relative to the control group. There was no significant effect of treatment on apoptotic indices computed from caspase-3 slides.

Groups	[a] Cell Density Index	[b] Significance	[c] Apoptotic Index	[b] Significance
Controls	0.242±0.014		0.0341±0.003	
Daily Dose	0.166±0.009	$p < .050$	0.0344±0.004	$p > .050$
Pulsed Dose	0.145±0.008	$p < .050$	0.0321±0.004	$p > .050$

Table 4.1 Histology and Immunohistochemistry results in gefitinib treatment study.
[a] Cell density index derived from H&E slides as the ratio of the area occupied by cells in a given field to the total field area, revealed that both gefitinib treatment groups were significantly less dense than the control group. Means and standard error are provided for each group in the gefitinib treatment study.

[b] *p*-values reflect difference from controls

[c] An apoptotic index derived from caspase-3 stained slides as the ratio of apoptosis stained cells in a given field to the total number of cells in the field, revealed no significant differences in apoptosis between groups in the gefitinib treatment study.

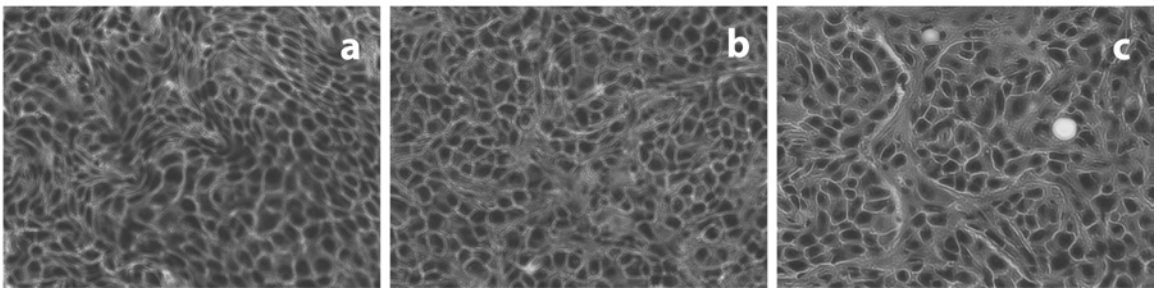

Figure 4.11 H&E stains in the gefitinib treatment study (400X) Representative H&E stains of harvested tumor tissue for all three groups in the gefitinib treatment study are displayed at original magnification 400X: (a) control group (b) daily treatment group (c) pulsed treatment group. Gefitinib treatment resulted in significantly lower cell density in the treated groups but the treated groups were not significantly different from each other. Table 4.1 lists quantitative differences between the groups. Greater inter-nuclear space was observed in the gefitinib treated groups.

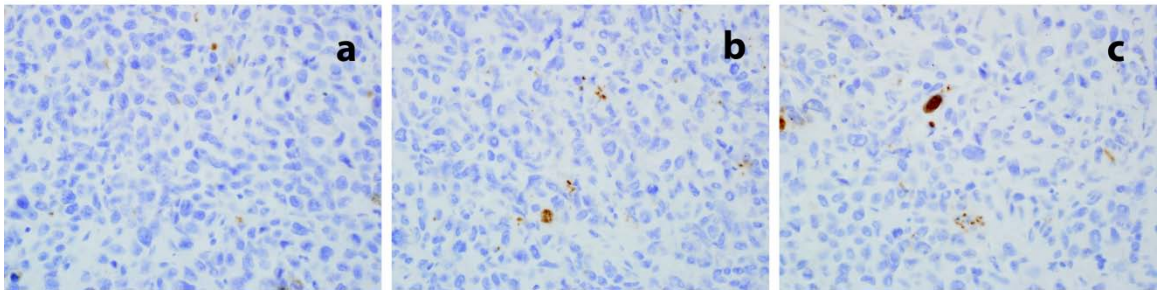

Figure 4.12 Caspase-3 stains in the gefitinib treatment study (400X). Representative anti-cleaved capsase-3 stains of harvested tumor tissue for all three groups in the gefitinib treatment study are displayed at original magnification 400X: (a) control group (b) daily treatment group (c) pulsed treatment group. Minimal apoptotic activity was detected in all three groups but no significant differences were detected between any groups. Table 4.1 lists quantitative differences between groups.

4.4 Discussion

To my knowledge, the present study is the first to characterize the untreated BT474 human breast tumor model using MRI parameters as I have reported in the natural history measurements of mean tumor volume, ADC and T_1. I observed that the mean tumor ADC remained relatively constant over the course of the 14-day natural history study. The ADC is sensitive to differences in tissue cellularity and microstructure. Thus, other factors held constant, it might be expected that increasing cellularity—anticipated by the lack of any intervention in the natural history and supported by exponential growth in mean tumor volume—would induce decreasing water mobility and consequently decreasing ADC values. One explanation for this seeming discrepancy is tissue necrosis; necrotic regions by definition are characterized by lower cellularity, favoring greater water mobility. Although I made efforts to isolate necrotic pixels from ADC analysis, there may be residual effects of necrotic pixels which could moderately inflate reported ADC values.

In the natural history study, I observed that mean tumor T_1 values remained relatively constant after a slight decrease from baseline to day 2. A similar trend was observed in the control group of the gefitinib treatment study. Pre-contrast tumor T_1 is a fundamental variable in the pharmacokinetic modeling of DCE-MRI data and my characterization of the T_1 time course in the BT474 xenograft tumor model can potentially serve to inform the analysis of future DCE-MRI studies using the BT474 xenograft tumor model.

Mean tumor volumes distinguished the gefitinib treated groups from the control group; tumor growth was significantly inhibited in both gefitinib treated groups relative to the control group, suggesting an effect due to gefitinib administration. Mean tumor volumes did not distinguish the gefitinib treatment groups from each other but there was a small reduction in mean tumor volume uniquely observed in the pulsed dose group. This trend is consistent with studies by Moasser et al [29] and Solit et al [30], where they report that pulsatile gefitinib treatment yields greater mean tumor regression and a higher percentage of complete responses than other schedules. Of note, the studies by Moasser et al and Solit et al followed gefitinib with paclitaxel—a cytotoxic agent—whereas the present study examined gefitinib alone and not in concert with any cytotoxic agents.

The gefitinib treatment study revealed a trend of increasing mean tumor ADC in the gefitinib treated groups while mean tumor ADC decreased slightly in the control group. Microscopic analysis of H&E slides revealed that both gefitinib treated groups demonstrated significantly less cell density relative to the control group. The ADC has been demonstrated to correlate inversely with tumor cellularity [12, 18, 31]. My finding of increasing mean tumor ADC and less cell density in the gefitinib treated groups is in agreement with studies by other investigators [14-17, 20] reporting higher ADC and lower cellularity in treated tumors.

DCE-MRI parameters revealed some unexpected but interesting findings. Mean tumor transendothelial permeability, K^{ps}, was unable to statistically distinguish the treatment groups but observed trends revealed an initial reduction in the pulsed dose group followed by a rebound, an increase over time in the daily dose group and a slight reduction over time in controls. K^{ps} is a measure of the transfer between the vascular and interstitial spaces. Multiple studies, including studies evaluating VEGF-targeted therapies, have reported reduced K^{ps} in response to effective anti-angiogenic therapy [10, 32-35]. Such reduction in K^{ps} is thought to reflect a reduction in the leakiness of microvessels. Gefitinib belongs to a class of inhibitors that are capable of targeting HER TKs, which are implicated in endothelial cell signaling and may have anti-angiogenic activity [36]. The trend towards an initial reduction in K^{ps} observed in the pulsed dose group is consistent with results from studies evaluating VEGF-targeted therapies. However the subsequent rebound in the pulse dose group and the trend towards increasing K^{ps} observed in the daily dose group, are unlike findings from studies evaluating VEGF-targeted therapies. One possible explanation for these trends follows from considering the potential effects of dose and timing in the present study. The trend towards a reduction in K^{ps} measured in the pulsed dose group was observed directly following two high dose pulses of gefitinib. It is plausible that high dose pulses of gefitinib might induce a trend towards reduction in microvessel leakiness over a transient window. It should be noted that a trend towards a slight reduction in K^{ps} was also observed in the control group and there was no statistical significance between or within groups. Future studies with larger sample sizes will be necessary to thoroughly investigate these trends.

Gefitinib treated groups were not statistically distinguishable from the control group by mean tumor fractional plasma volume, fPV. Observed trends revealed an increase in both gefitinib treatment groups between baseline and day 4, with the pulsed dose group showing a decrease afterwards. Such increases in mean tumor fPV are unlike trends observed in studies evaluating VEGF-targeted therapies where mean tumor fPV decreased or remained unchanged [33, 34, 37]. Although these trends were not statistically significant, it is possible that HER TKIs as a class of inhibitors possess vascular characteristics that are distinct from VEGF-targeted therapies. One explanation for fPV increases following anti-angiogenic therapy is a shift to larger vessels to compensate for the pruning of smaller leakier vessels [38]. In previous work, I reported improved vascular architecture—measured by anti-CD31 stains—from gefitinib administration [29].

In conclusion, although these findings are limited by the scope, design and a small sample size in the present study, I show that the MRI parameters ADC, K^{ps}, fPV and MRI-measured tumor volume are potentially sensitive to gefitinib induced changes in a human breast xenograft model. Changes detected by ADC measurements and DCE-MRI represent different physiological mechanisms and may thus provide complementary information on the timing and nature of the effects of different gefitinib treatment strategies on tumors. These results support further exploration of these MRI measures as non-invasive biomarkers of HER TKI-induced treatment effects.

4.5 References

1. Yarden, Y., *The EGFR Family and its Ligands in Human Cancer. Signaling Mechanisms and Therapeutic Opportunities.* Eur J Cancer, 2001. **37**(Suppl 4): p. 3-8(6).
2. Rose-Hellekant, T.A. and E.P. Sandgren, *Transforming growth factor alpha- and c-myc-induced mammary carcinogenesis in transgenic mice.* Nature, 2000. **19**(8): p. 1092-1096.
3. Ellis, L.M., *Epidermal Growth Factor Receptor in Tumor Angiogenesis.* Hematol. Oncol. Clin. North Am., 2004. **18**(5): p. 1007-1021.
4. Kumar, R. and R. Yarmand-Bagheri, *The Role of HER2 in Angiogenesis.* Semin Oncol, 2001. **28**(5 Suppl 16): p. 27-32.
5. Moasser, M.M., et al., *The Tyrosine Kinase Inhibitor ZD1839 ("Iressa") Inhibits HER2-driven Signaling and Suppresses the Growth of HER2-overexpressing Tumor Cells.* Cancer Res, 2001. **61**(19): p. 7184-7188.
6. Moulder, S., et al., *Epidermal Growth Factor Receptor (HER1) Tyrosine Kinase Inhibitor ZD1839 (Iressa) Inhibits HER2/neu (erbB2)-overexpressing Breast Cancer Cells in Vitro and in Vivo.* Cancer Res, 2001. **61**(24): p. 8887-8895.
7. Ciardiello, F., et al., *Antitumor Effect and Potentiation of Cytotoxic Drugs Activity in Human Cancer Cells by ZD-1839 (Iressa), an Epidermal Growth Factor Receptor-selective Tyrosine Kinase Inhibitor.* Clin Cancer Res, 2000. **6**(5): p. 2053-63.
8. Sirotnak, F.M., et al., *Efficacy of Cytotoxic Agents against Human Tumor Xenografts is Markedly Enhanced by Coadministration of ZD1839 (Iressa), an Inhibitor of EGFR Tyrosine Kinase.* Clin Cancer Res, 2000. **6**(12): p. 4885-4892.
9. Sergina, N.V., et al., *Escape from HER-family tyrosine kinase inhibitor therapy by the kinase-inactive HER3.* Nature, 2007. **445**(7126): p. 437-441.
10. Turetschek, K., et al., *MRI monitoring of tumor response following angiogenesis inhibition in an experimental human breast cancer model.* Eur J Nucl Med Mol Imaging, 2003. **30**(3): p. 448 -455.
11. Neil, J.J., *Measurement of Water Motion(Apparent Diffusion) in Biological Systems.* Concepts Magn Reson, 1997. **9**(6): p. 385-401.
12. Gupta, R.K., et al., *Relationships Between Choline Magnetic Resonance Spectroscopy, Apparent Diffusion Coefficient and Quantitative Histopathology in Human Glioma.* J Neurooncol, 2000. **50**(3): p. 215-226.
13. Gupta, R.K., et al., *Inverse correlation between choline magnetic resonance spectroscopy signal intensity and the apparent diffusion coefficient in human glioma.* Magn Reson Med, 1999. **41**(1): p. 2-7.
14. Pickles, M.D., et al., *Diffusion changes precede size reduction in neoadjuvant treatment of breast cancer.* Magn Reson Med, 2006. **24**(7): p. 843-847.
15. Yankeelov, T.E., et al., *Integration of quantitative DCE-MRI and ADC mapping to monitor treatment response in human breast cancer: initial results.* Magn Reson Imaging, 2007. **25**(1): p. 1-13.
16. Galons, J.-P., et al., *Early Increases in Breast Tumor Xenograft Water Mobility in Response to Paclitaxel Therapy Detected by Non-invasive Diffusion Magnetic Resonance Imaging.* Neoplasia, 1999. **1**(2): p. 113-117.
17. Rubesova, E., et al., *Quantitative diffusion imaging in breast cancer: A clinical prospective study.* J Magn Reson Imaging, 2006. **24**(2): p. 319-324.

18. Guo, Y., et al., *Differentiation of clinically benign and malignant breast lesions using diffusion-weighted imaging.* J Magn Reson Imaging, 2002. **16**(2): p. 172-178.
19. Kuroki, Y., et al., *Diffusion-weighted imaging of breast cancer with the sensitivity encoding technique: analysis of the apparent diffusion coefficient value.* Magn Reson Med Sci, 2004. **3**(2): p. 79-85.
20. Woodhams, R., et al., *Diffusion-Weighted Imaging of Malignant Breast Tumors: The Usefulness of Apparent Diffusion Coefficient (ADC) Value and ADC Map for the Detection of Malignant Breast Tumors and Evaluation of Cancer Extension.* J Comput Assist Tomogr, 2005. **29**(5): p. 644-649.
21. Padhani, A.R., *MRI for assessing antivascular cancer treatments.* Br J Radiol, 2003. **76**(1): p. S60-80.
22. Knopp, M.V., et al., *Pathophysiologic basis of contrast enhancement in breast tumors.* J Magn Reson Imaging, 1999. **10**(3): p. 260-266.
23. Su, M.-Y., Z. Wang, and O. Nalcioglu, *Investigation of longitudinal vascular changes in control and chemotherapy-treated tumors to serve as therapeutic efficacy predictors.* J Magn Reson Imaging, 1999. **9**(1): p. 128-137.
24. Taylor, J.S., et al., *MR imaging of tumor microcirculation: Promise for the new millenium.* J Magn Reson Imaging, 1999. **10**(6): p. 903-907.
25. Turetschek, K., et al., *Tumor microvascular changes in antiangiogenic treatment: Assessment by magnetic resonance contrast media of different molecular weights.* J Magn Reson Imaging, 2004. **20**(1): p. 138-144.
26. Partridge, S.C., et al., *Menstrual cycle variation of apparent diffusion coefficients measured in the normal breast using MRI.* J Magn Reson Imaging, 2001. **14**(4): p. 433-438.
27. Bezdek, J.C., *Pattern Recognition with Fuzzy Objective Function Algorithm*. 1981, New York: Plenum.
28. Klifa, C., et al. *Quantification of breast tissue index from MR data using fuzzy clustering*. in *26th Annual International Conference of the IEEE EMBS*. 2004. San Franicsco, CA, USA.
29. Moasser, M., et al., *Improved tumor vascular function following high dose epidermal growth factor receptor tyrosine kinase inhibitor therapy.* J Magn Reson Imaging, 2007. **26**(6): p. 1618-1625.
30. Solit, D.B., et al., *Pulsatile Administration of The Epidermal Growth Factor Receptor Inhibitor Gefitinib is Significantly more Effective than Continuous Dosing for Sensitizing Tumors to Paclitaxel.* Clin Cancer Res, 2005. **11**(5): p. 1983-1989.
31. Lyng, H., O. Haraldseth, and E.K. Rofstad, *Measurement of cell density and necrotic fraction in human melanoma xenografts by diffusion weighted magnetic resonance imaging.* Magn Reson Med, 2000. **43**(6): p. 828-836.
32. Checkley, D., et al., *Use of dynamic contrast-enhanced MRI to evaluate acute treatment with ZD6474, a VEGF signalling inhibitor, in PC-3 prostate tumours.* Br J Cancer, 2003. **89**(10): p. 1889-1895.
33. Li, K.-L., et al., *Heterogeneity in the angiogenic response of a BT474 human breast cancer to a novel vascular endothelial growth factor-receptor tyrosine kinase inhibitor: Assessment by voxel analysis of dynamic contrast-enhanced MRI.* J Magn Reson Imaging, 2005. **22**(4): p. 511-519.

34. Marzola, P., et al., *Early Antiangiogenic Activity of SU11248 Evaluated In vivo by Dynamic Contrast-Enhanced Magnetic Resonance Imaging in an Experimental Model of Colon Carcinoma.* Clin Cancer Res, 2005. **11**(16): p. 5827-5832.
35. Pham, C.D., et al., *Magnetic resonance imaging detects suppression of tumor vascular permeability after administration of antibody to vascular endothelial growth factor.* Cancer Invest, 1998. **16**(4): p. 225-230.
36. Viloria-Petit, A., et al., *Acquired resistance to the antitumor effect of epidermal growth factor receptor-blocking antibodies in vivo: A role for altered tumor angiogenesis.* Cancer Res, 2001. **61**(13): p. 5090-5101
37. Pradel, C., et al., *Reduced capillary perfusion and permeability in human tumour xenografts treated with the VEGF signalling inhibitor ZD4190: an in vivo assessment using dynamic MR imaging and macromolecular contrast media.* Magn Reson Imaging, 2003. **21**(8): p. 845 - 851.
38. Drevs, J., et al., *PTK787/ZK 222584, a Specific Vascular Endothelial Growth Factor-Receptor Tyrosine Kinase Inhibitor, Affects the Anatomy of the Tumor Vascular Bed and the Functional Vascular Properties as Detected by Dynamic Enhanced Magnetic Resonance Imaging.* Cancer Res, 2002. **62**(14): p. 4015-4022.

CHAPTER 5

Diffusion Tensor Imaging in Breast Cancer

The following chapter describes the results of a clinical study investigating the added value of diffusion MRI in the context of monitoring response to chemotherapy and exploring the potential benefit of diffusion tensor imaging in primary tumor chemotherapy treatment. The diffusion tensor was measured in normal fibroglandular breast tissue and in breast tumors before and after chemotherapy.

5.1 Background

About 85% of breast tumors originate in the ducts of the breast [1]. Cells of the ductal epithelium disrupt the ductal network as they proliferate. Such disruption results in alterations to the water diffusion properties of the ductal tissue, affecting the rate and possibly the directionality of water diffusion, otherwise known as diffusion anisotropy.

Diffusion-weighted MRI has been used extensively to estimate the rate of water diffusion in the breast and other body organs. This rate, expressed as the apparent diffusion coefficient (ADC), has been inversely correlated with cell density and tumor grade [2, 3], making the ADC a potentially useful parameter for distinguishing between malignant and benign lesions and for characterizing tumors. However to date there are no systematic studies examining water diffusion anisotropy in the breast or investigating any potential role diffusion anisotropy might play in characterizing breast tumors or assessing treatment response.

Diffusion anisotropy has been used to identify abnormalities and elucidate microstructure in other body organs, especially the brain and spine where diffusion anisotropy is routinely exploited for fiber orientation mapping and visualization of anatomic connections. The premise for such application is that barriers to water diffusion are differential across, versus along, neural fibers, giving rise to directionally preferential diffusion. The tubular morphology of individual ducts in the breast and the arrangement of the ductal tree such that ducts course anteriorly towards the nipple, make it plausible that directionally preferential diffusion might occur, especially in the presence of barriers within the ducts. It should be noted that neural fibers range in diameter from 1 μm to 6 μm while breast ducts are significantly larger, ranging in diameter from 0.5 mm to 2 mm [4-7].

Over the course of a diffusion experiment, water protons require adequate time to interact with sources of anisotropy such as directional barriers. In the event that the diffusion experiment does not allow sufficient diffusing time, it is likely that detected anisotropic behavior will be restricted to faster diffusing protons. Hence, it was an aim of this study to observe the effect of diffusion

time on detected anisotropy. Normal breast tissue was characterized according to the magnitude of diffusion and diffusion anisotropy. Similar measurements were taken in breast tumors for comparison. Subsequent to this, the effect of diffusion time on diffusion anisotropy was studied both in normal fibroglandular breast tissue and in breast tumors.

The normal breast duct is comprised of an inner layer (luminal) of epithelial cells packed in ordered fashion around the lumen and an outer layer (basal) of myoepithelial cells, also packed in relatively ordered fashion around a basement membrane. As protons undergo random displacements in this environment, the ordered arrangement of both layers of the ductal epithelium likely gives rise to anisotropic displacement. To illustrate this, it is instructive to consider the trajectory of protons within this environment. Probabilistically, for a large enough sample of protons, the net displacement vector will be oriented along the direction of ordered packing since the motion of individual protons is less restricted in this direction. As the amount of time protons are allowed to diffuse is increased, it is expected that the inherent order of the ductal epithelium will force more protons to travel along the direction of ordered packing, resulting in greater anisotropy.

The natural history of breast cancer involves progression through stages, beginning with ductal hyper-proliferation, subsequent evolution into in situ and invasive carcinomas and finally metastatic disease [8-10]. Proliferation follows a random course and introduces disorder to the inherent ordered packing of cells in the ductal epithelium. Order is a key source of anisotropy and such loss of order likely leads to decreased anisotropy. At the stage of in situ carcinoma, epithelial cells proliferate within the lumen and there is a gradual erosion of the myoepithelial cell layer [11], paving the way for proliferating cells to escape the duct and invade neighboring tissue. Note that the diagnostic criterion distinguishing invasive carcinoma from in situ carcinoma is the degradation of the myoepithelial cell layer as an organized entity [11]. While it is possible that at the stage of in situ carcinoma, ducts might retain a certain amount of order in the arrangement of myoepithelial cells, this is less likely with invasive carcinoma where proliferating cells have breached the basement membrane and escaped the duct. The current study focused on anisotropy in invasive carcinoma because at this stage, the ductal profile of breast cancer hypothetically provides the greatest contrast to that of normal breast tissue: greater cell density and disordered cellular arrangement contrasted with normal fibroglandular breast tissue where there is relatively lower cell density and more ordered cellular arrangement.

Chemotherapy affects the dynamics described above. In simplistic terms, the effect of chemotherapy is a net reduction in cell density. It has been demonstrated that effective chemotherapy results in an increase in the ADC. The impact of effective chemotherapy on the FA will depend on whether such reduction of cell density restores order to the ductal epithelium or further disorganizes it.

The different anisotropic properties of normal fibroglandular breast tissue and breast tumors at different cancer stages and with treatment, raises the possibility that diffusion anisotropy might be useful in characterizing breast tumors. The present study hypothesized that disruption of the breast ductal network by invading cancer cells may result in alterations to the water diffusion properties of these tissues which might be reflected by DTI parameters. Measurements of the

ADC and fractional anisotropy (FA) were taken in normal fibroglandular breast tissue and in breast tumors.

5.2 Methods

5.2.1 Subjects and Treatment

The study included 24 women with Stage 3 locally advanced breast cancer, recruited from a pool of patients already scheduled for treatment at the University of California in San Francisco. Institutional review boards at the University of California in San Francisco and Berkeley approved the study protocol, and all subjects provided informed consent. All patients had invasive breast cancer diagnosed by core biopsy or fine needle aspiration and were scheduled to undergo neoadjuvant chemotherapy. The chemotherapy regimen for all patients consisted of an anthracycline-cyclophosphamide followed by a taxane. All patients were imaged with MRI prior to the commencement of treatment (pre-treatment); after the first cycle of chemotherapy (early treatment); between chemotherapy regimens (inter-regimen); and prior to surgery (pre-surgery).

5.2.2 MRI Acquisition

Imaging was performed on a 1.5 T Signa scanner (GE Healthcare, Milwaukee, WI) using a bilateral 8-channel array breast coil (Sentinelle Medical, Toronto, Canada). Contrast enhanced images were used to identify breast lesions. A T_1-weighted 3D fast gradient recalled echo pulse sequence (TR/TE 9/4.4, flip angle 10°) was used for contrast enhanced imaging. The field of view used was in the range 28—38 cm, with 1 mm slice thickness, an acquisition matrix of 512 x 320 and slices selected to cover the entire affected breast. The contrast agent used was gadopentetate dimeglumine or Gd-DPTA (Magnevist; Schering, Berlin, Germany) at a dose of 0.1 mmol/kg body weight. The scan time was 5.2 min, with the low order phase encoding data acquired at the center of the scan. At least three time points were acquired during each MRI examination: a pre-contrast scan, an early post-contrast scan, late post-contrast scan(s), yielding a minimum temporal sampling of 0, 2.6, and 7.9 min.

To test the hypothesis that differences due to anisotropy might be more evident at longer diffusion times, diffusion weighted images in six directions were acquired at two diffusion times, in two separate scans, using an echo planar imaging (EPI) spin echo pulse sequence. Diffusion weighted images were acquired first at a short diffusion time of 19 ms and subsequently at a long diffusion time of 43 ms, keeping the echo time constant (see Figure 5.1).

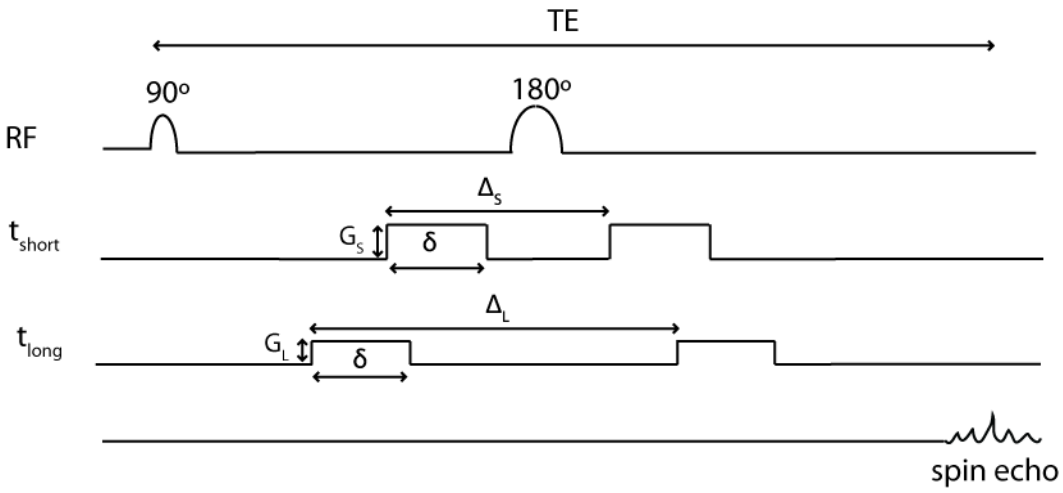

Figure 5.1 Schematic illustrating diffusion acquisition at a short (t_{short}) and long (t_{long}) diffusion time. The gradient strength was adjusted between the short diffusion time (G_S = 4.84 Gauss/cm) and the long diffusion time (G_L = 2.42 Gauss/cm). The duration of the diffusion gradient pulse was kept constant between both diffusion times (δ = 18 ms). The timing between both diffusion gradients was adjusted between the short diffusion time (Δ_S = 27 ms) and the long diffusion time (Δ_L = 49 ms). The echo time was kept constant at both diffusion times (TE = 108 ms).

The same field of view used for contrast enhanced images was used for diffusion weighted images and imaging parameters were kept identical at both diffusion times: TR/TE 6000/108 ms, slice thickness 3 mm, acquisition matrix 128 x 128 and b value 600 s/mm^2. The b value of the images acquired at both diffusion times was matched by decreasing the diffusion gradient strength in the case of the long diffusion time. Similarly, the echo time of the images acquired at both diffusion times was matched by adjusting the placement of the diffusion gradient pulses. These changes required modifications to the pulse sequence using the manufacturer's software (Epic; GE Healthcare, Milwaukee, WI). Slices (10–20) were selected to cover the tumor or most prominent lesion in the case of diffuse tumors.

5.2.3 MRI Postprocessing

Contrast uptake—captured in the percentage of enhancement (PE)—in the breast was calculated on a voxel-by-voxel basis and used to identify lesions. First, maximum intensity projections were generated in the lateromedial, craniocaudal, and anteroposterior directions for each time point. Such projections allow for rapid multi-dimensional determination of tumor extent. Next, a restricted volume to be evaluated is defined on two orthogonal projections. The purpose of the restricted region is to exclude enhancement from large blood vessels and other interfering regions such as skin and the chest wall. The enhancement threshold (70% or greater enhancement from pre-contrast to early post-contrast) was then applied on a voxel-by-voxel basis within the restricted volume. To improve the specificity of distinguishing benign lesions from malignant lesions, the signal enhancement ratio (SER) which compares early to late enhancement, was computed on a voxel-by-voxel basis, to identify washout. Voxels possessing high SER values were summed and constituted the 3D tumor volume (see Figure 5.2 for illustration).

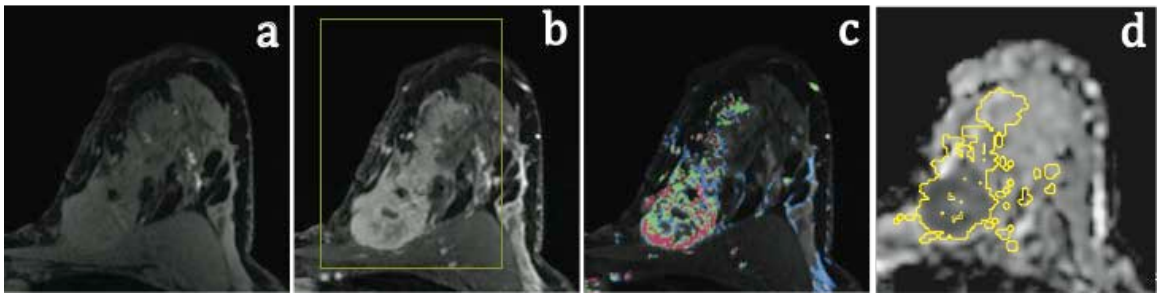

Figure 5.2 Using SER to identify lesions and outline regions-of-interest on parametric diffusion maps (a) Representative T_1-weighted pre-contrast image. (b) Corresponding early contrast enhanced image. The enhancement region gives a good approximation of tumor extent. A restricted region (yellow box) was manually created on maximum intensity projections (not shown) to exclude large blood vessels and interfering regions of enhancement, such as skin and the chest wall, from the tumor volume analysis. The enhancement threshold (70% or greater enhancement relative to the pre-contrast level) was applied on a voxel-by-voxel basis within this restricted region. (c) SER color map superimposed on T_1 weighted image. The ratio of early to late enhancement, or wash-in to wash-out, was used to improve specificity in identifying malignant lesions. Voxels satisfying the enhancement threshold were further segmented into bottom (blue: SER < 0.9), low (purple: $0.9 \leq$ SER < 1.0), moderate (green: 1.0 < SER $\leq$ 1.3) and high (red and white: SER > 1.3). Low SER values correspond to lesions that enhance quickly and continue to enhance slowly; moderate values correspond to lesions that enhance quickly and stabilize; high values correspond to lesions that enhance quickly and wash out. (d) ADC map showing SER derived tumor volume. Regions with voxels with SER values greater than 1.0 were converted to contours which constitute the regions-of-interest (ROI) on parametric diffusion maps.

Parametric diffusion maps were generated by diagonalizing the diffusion tensor [12] using in-house software. To compare normal fibroglandular tissue in the unaffected breast to malignant tissue in the affected breast, it was necessary to segment the unaffected breast, i.e. isolate fibroglandular tissue from adipose tissue. A fuzzy c-means clustering algorithm [13] was applied to the unaffected breast. In brief, splines were used to outline the breast (excluding skin) on non-contrast enhanced 3D T_1-weighted images (see Figure 5.3a). The outlined regions and the desired number of clusters were fed into the clustering algorithm which maximized tissue differentiation while minimizing intra-cluster variance, outputting clustered images (see Figure 5.3b). The clustered images were then visually inspected against the non-contrast enhanced images to classify clusters as fibroglandular or adipose tissue. Clusters classified as fibroglandular tissue were subsequently converted into contours and served as regions-of-interest (ROIs) on parametric diffusion maps (see Figure 5.3 for illustration).

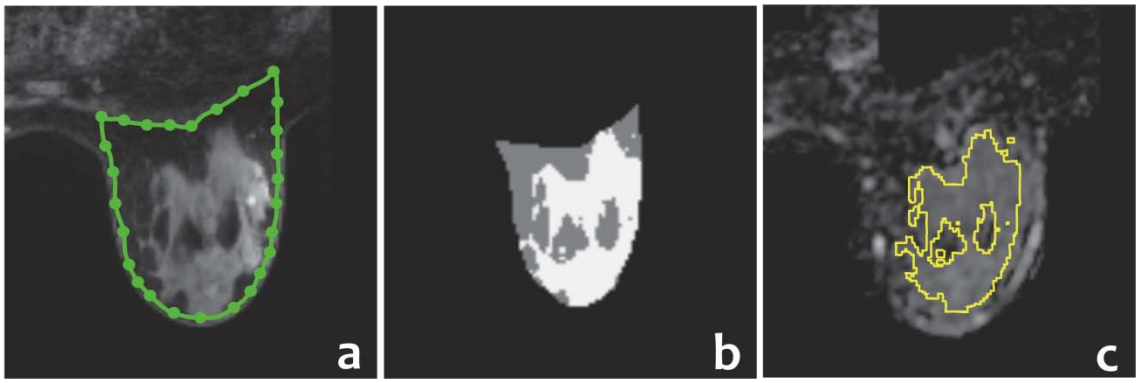

Figure 5.3 Using fuzzy c-means to segment the fibroglandular breast tissue and outline regions-of-interest on parametric diffusion maps (a) Breast tissue outlined on T_1 weighted image. Splines were manually placed on pre-contrast 3D T_1-weighted images to generate an outline of the breast. Care was taken to avoid the skin and chest wall. All cases were completed by a single operator to ensure consistency. (b) Clustered image output from fuzzy c-means algorithm. The spline–outlined breast region and desired number of clusters (two: fibroglandular and adipose tissue clusters) were fed into a fuzzy c-means clustering algorithm which outputted clustered images. The white region corresponds to fibroglandular tissue and the grey region corresponds to adipose tissue. (c) Region-of-interest on the ADC map. The cluster corresponding to fibroglandular tissue was contoured and served as the region-of-interest on parametric diffusion maps.

Generated ROIs were visually inspected to ensure tissue features of interest were in fact captured. Patient motion between the acquisition of diffusion and T_1 weighted images, was detected in 40/68 exams, resulting in translational, affine or deformative ROI misregistration. Exams exhibiting translational misregistration were manually registered. A non-rigid registration algorithm [14] was applied to exams exhibiting affine and deformative misregistration, with limited success. These exams (19/68) were subsequently excluded from further analysis.

To assess the distribution of diffusion parameters in normal breast tissue and breast cancer, histograms of parametric diffusion maps were generated using voxels classified as tumor (in the affected breast) or normal fibroglandular tissue (in the unaffected breast). Histograms were pooled across subjects; histogram mean and peak locations were considered for statistical analysis.

5.2.4 Statistics

A repeated measures analysis of variance (ANOVA) design was used to investigate the effects of chemotherapy treatment and diffusion time on diffusion parameters measured during the four serial MRI visits. MRI visits served as the within-subjects factor while diffusion time (short versus long) and breast tissue type (normal fibroglandular tissue versus breast tumor) served as between-subject factors. Student t-tests with Bonferroni correction for multiple comparisons were used for post-hoc analysis. Pearson's correlation coefficient was used to probe for correlation between diffusion parameters and tumor volume. To assess the cumulative impact of chemotherapy, measurements following chemotherapy were averaged. JMP (v. 8; SAS, Cary, NC) was used for all statistics.

5.3 Results

5.3.1 Diffusion Time Effect

Prior to any intervention, I observed a shift towards higher values in the distribution of the ADC and FA as the diffusion time increased. The ADC histogram mean in normal fibroglandular tissue increased from 1714.60 (peak at 1887) × 10^{-3} mm^2/s at the short diffusion time to 1814.49 (peak at 2015) × 10^{-3} mm^2/s at the long diffusion time. The FA histogram mean increased from 0.383 (peak at 0.241) at the short diffusion time to 0.436 (peak at 0.279) at the long diffusion time (see Figure 5.4). However, these trends did not achieve statistical significance.

The ADC distribution in breast tumors was similar at both the short and long diffusion time but the FA distribution showed a shift towards higher values at the longer diffusion time. The ADC histogram mean was 1652.73 (peak at 1234) × 10^{-3} mm^2/s at the short diffusion time, and 1670.73 (peak at 1312) × 10^{-3} mm^2/s at the long diffusion time. The FA histogram mean was 0.265 (peak at 0.165) at the short diffusion time and 0.349 (peak at 0.199) at the long diffusion time (see Figure 5.5). Similar to the ADC distribution, these trends did not achieve statistical significance.

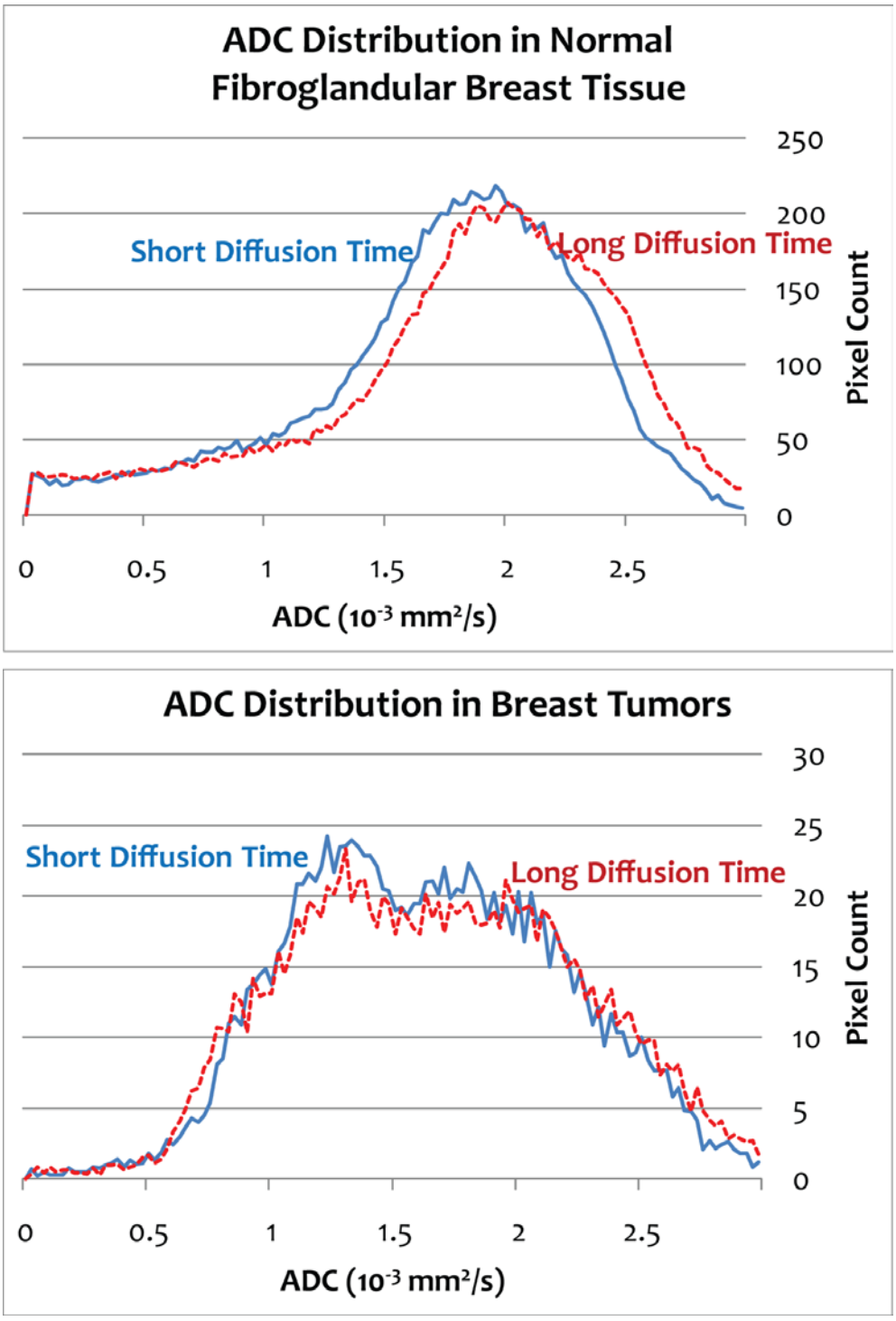

Figure 5.4 Diffusion time effect on ADC distribution. ADC distributions measured prior to any intervention at a short diffusion time (solid blue line) and long diffusion time (dotted red line) in normal fibroglandular tissue (top) and breast tumors (bottom). There was a trend towards higher values at measurements at the long diffusion time but no significant difference between both diffusion times.

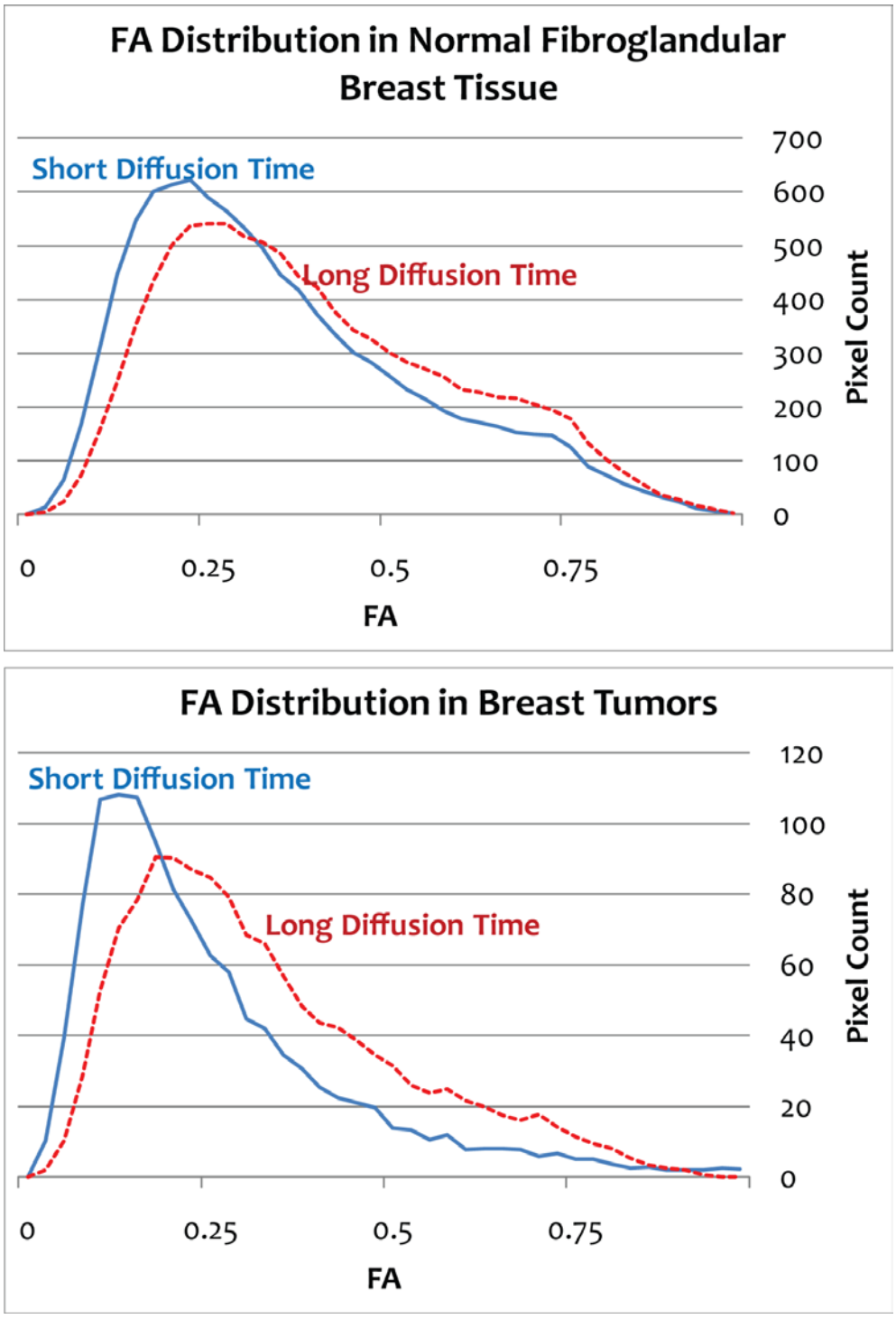

Figure 5.5 Diffusion time effect on FA distribution. FA distributions measured prior to any intervention at a short diffusion time (solid blue line) and long diffusion time (dotted red line) in normal fibroglandular tissue (top) and breast tumors (bottom). There was a trend towards higher values at measurements at the long diffusion time but no significant difference between both diffusion times.

5.3.2 Treatment Effect

I observed a modest effect due to treatment in the distribution of the ADC and FA after one cycle of chemotherapy. The ADC histogram mean increased from 1652.3 (peak at 1234) $\times 10^{-3}$ mm^2/s to 1667.57 (peak at 1302) $\times 10^{-3}$ mm^2/s at the short diffusion time and increased from 1670.73 (peak at 1312) $\times 10^{-3}$ mm^2/s to 1672.98 (peak at 1489) $\times 10^{-3}$ mm^2/s at the long diffusion time. See Figure 5.6.

The effect of treatment in the FA distribution was restricted to the longer diffusion time. The FA histogram mean decreased from 0.265 (peak at 0.165) pre-treatment to 0.234 (peak at 0.149) after one cycle of chemotherapy. See Figure 5.7.

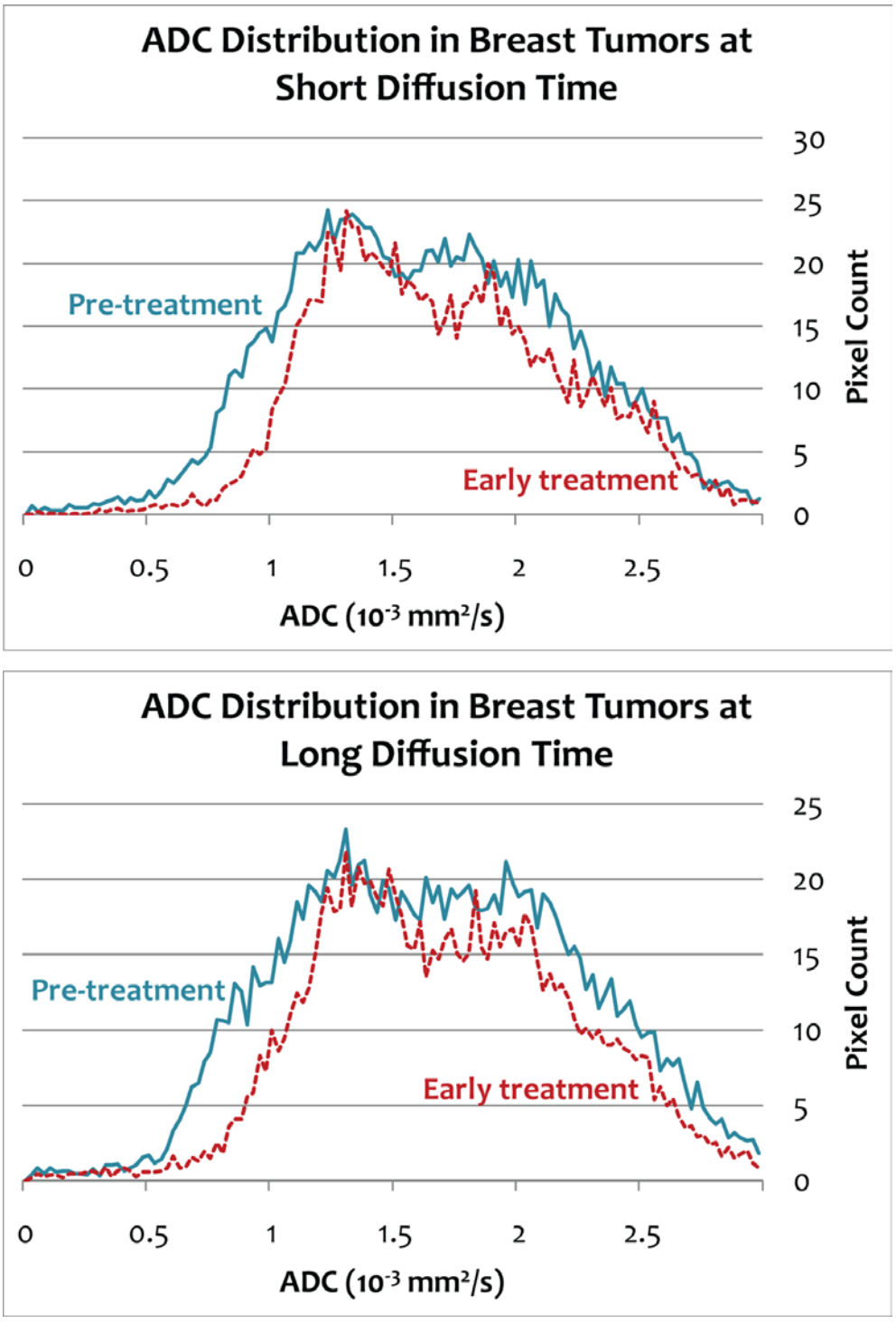

Figure 5.6 Treatment effect on ADC distribution. ADC distributions pre-treatment (solid green line) and after one cycle of chemotherapy (dotted red line) in breast tumors at a short diffusion time (top) and long diffusion time (bottom). There was a statistically significant shift towards higher values in the ADC distribution after one cycle of chemotherapy.

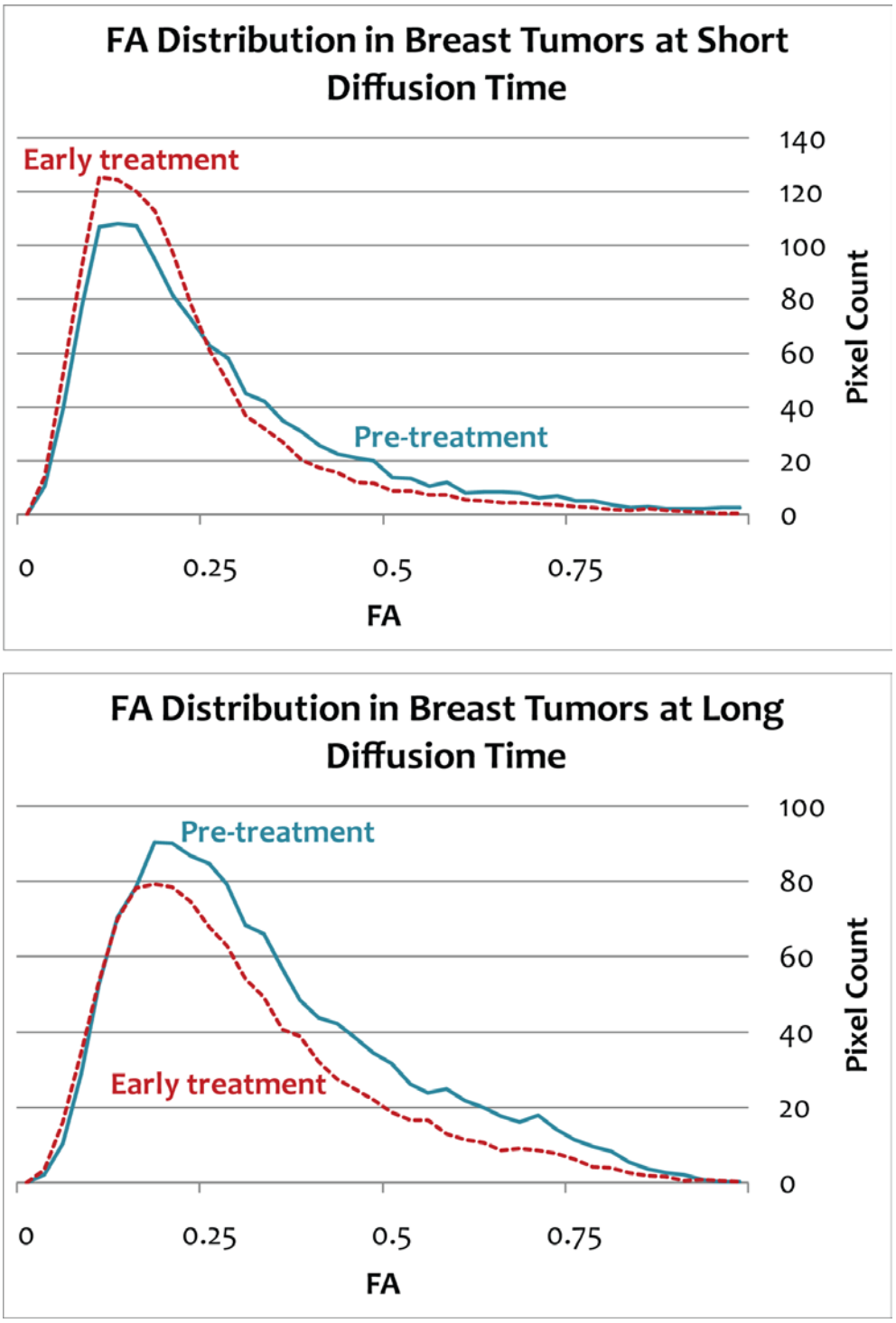

Figure 5.7 Treatment effect on FA distribution. FA distributions pre-treatment (solid green line) and after one cycle of chemotherapy (dotted red line) in breast tumors at a short diffusion time (top) and long diffusion time (bottom). There was a statistically significant shift towards lower values in the FA distribution at the long diffusion time, after one cycle of chemotherapy, but not at the short diffusion time.

5.3.3 Normal Fibroglandular Tissue versus Breast Cancer

The distribution of the ADC in normal fibroglandular tissue spanned a limited range of higher ADC values (~1 to 2.5 × 10^{-3} mm^2/s) in contrast to the distribution in breast tumors which spanned a wider range of low to high values (~0.5 to 2.5 × 10^{-3} mm^2/s). This trend was observed in pre-treatment and post-treatment measurements (see Figure 5.8).

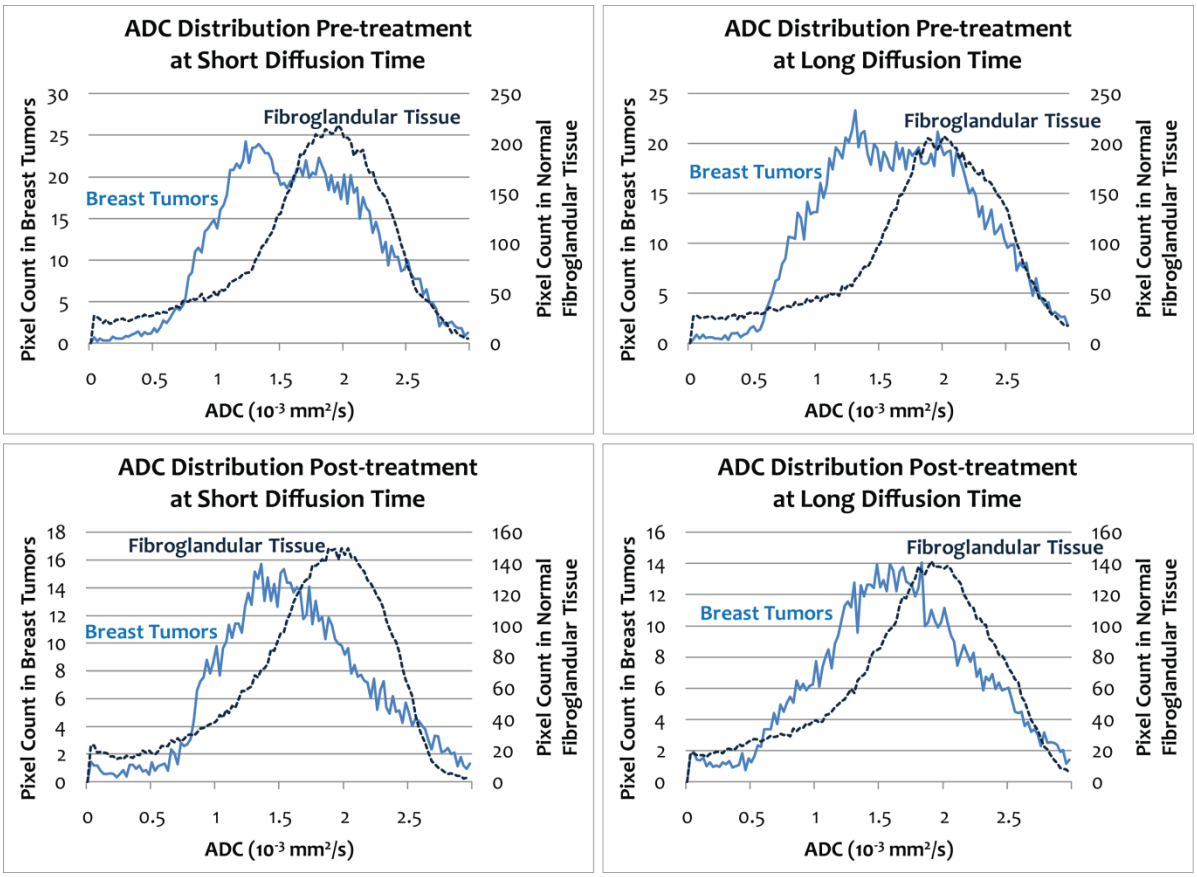

Figure 5.8 The ADC distributions in normal fibroglandular tissue (solid blue line) and breast tumors (dotted blue line) are shown for pre-treatment and post-treatment measurements at both diffusion times. The ADC distribution in the fibroglandular tissue generally spanned higher values relative to the distribution in the breast tumors. Note that measurements taken following chemotherapy treatment (early treatment and inter-regimen) were averaged to yield the post-treatment distribution. Also note different *y* axes for normal fibroglandular tissue and breast tumors.

The distribution of the FA in normal fibroglandular breast tissue also spanned a wider range of values (~0.1 to 0.75) relative to breast tumors (~0.1 to 0.55) in pre-treatment and post-treatment measurements. See Figure 5.9.

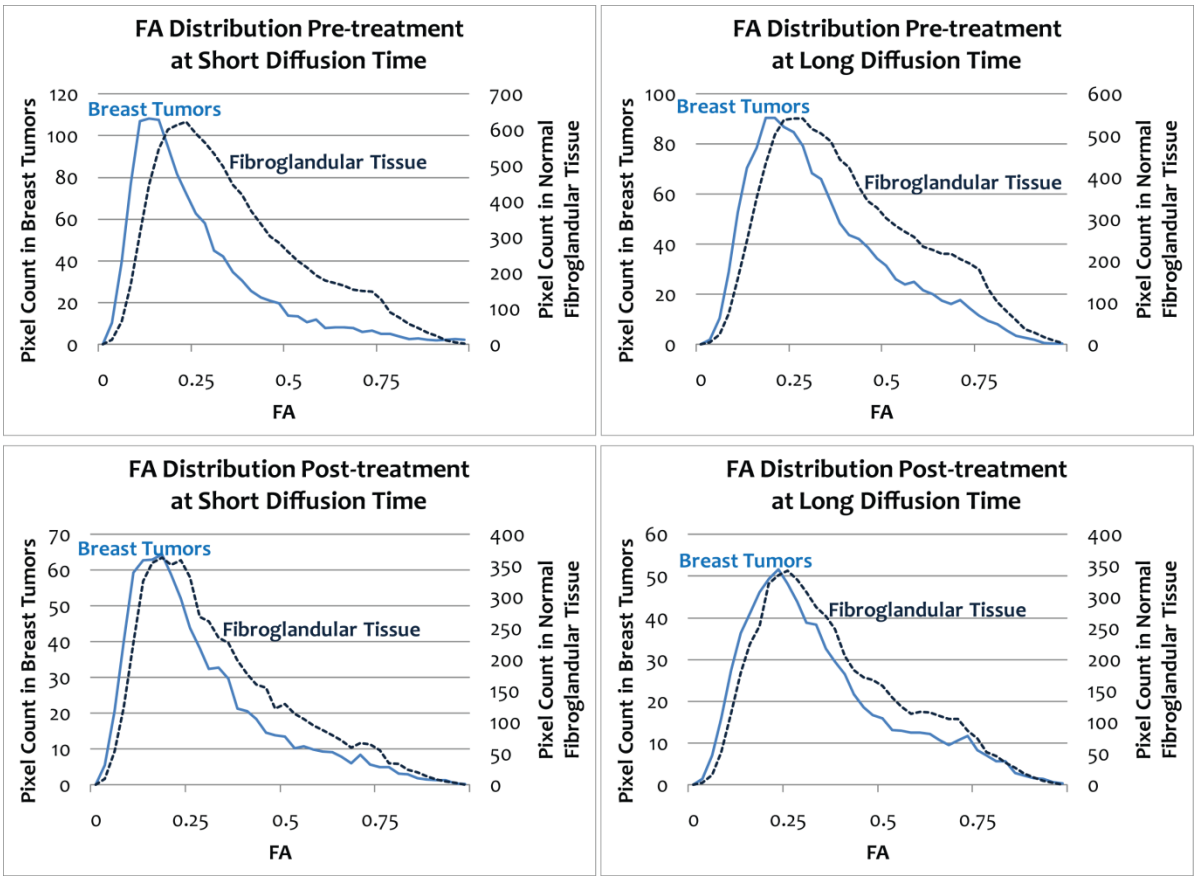

Figure 5.9 The FA distributions in normal fibroglandular tissue (solid blue line) and breast tumors (dotted blue line) are shown for pre-treatment and post-treatment measurements at both diffusion times. The FA distribution in fibroglandular tissue was shifted towards higher values relative to the distribution in the breast tumors in pre-treatment measurements. Note that measurements taken following chemotherapy treatment (early treatment and inter-regimen) were averaged to yield the post-treatment distribution. Also note different *y* axes for normal fibroglandular tissue and breast tumors.

5.3.4 Tumor Volume Change

Mean tumor volume as measured by MRI in the affected breast decreased by 4% after one cycle of chemotherapy, 73% after two cycles and by 69% overall. Figure 5.10 displays mean tumor volumes over the course of the study. Early change in the peak of the ADC distribution (change in the peak of the ADC distribution after one cycle of chemotherapy) in the affected breast was found to correlate weakly with overall change in mean tumor volume (r = 0.48).

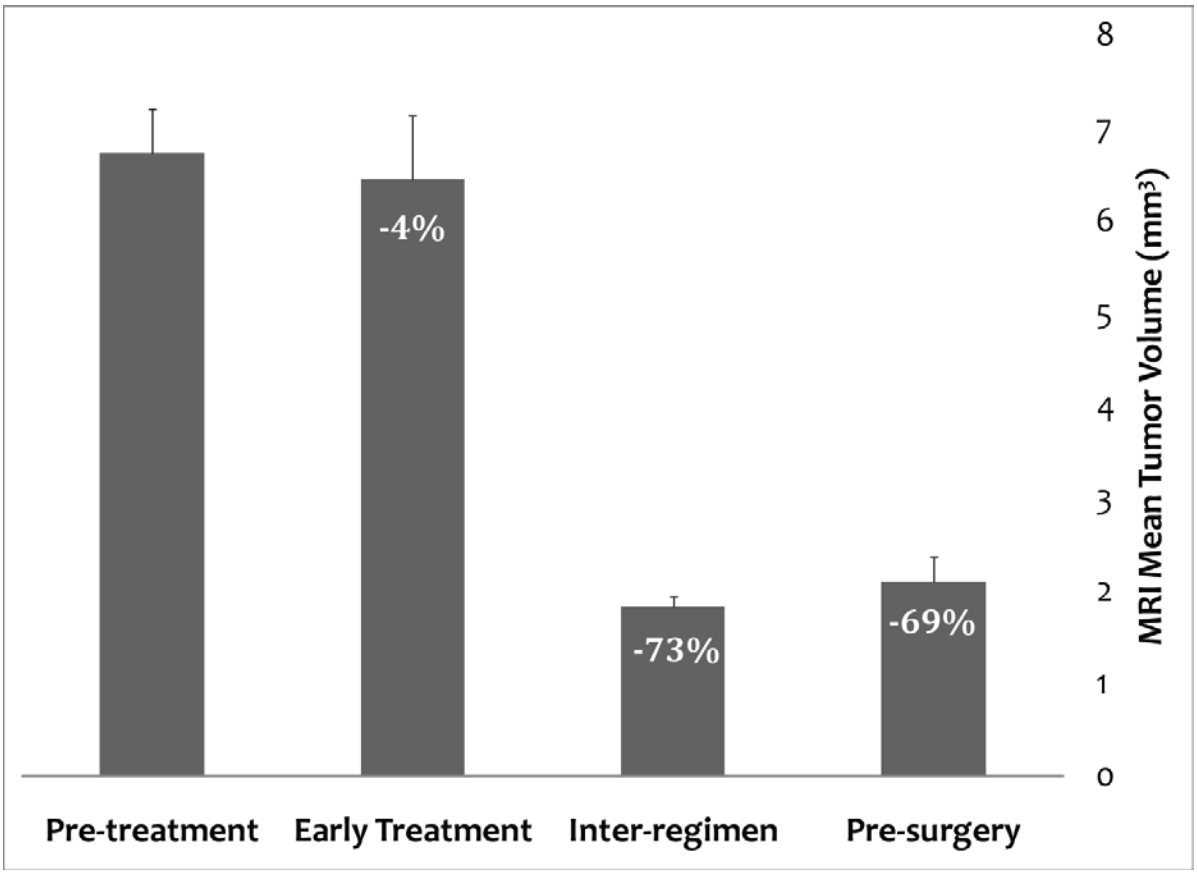

Figure 5.10 Mean MRI tumor volume pooled over all patients is shown for each MRI visit. There was a 4% mean decrease observed after the first cycle of chemotherapy (early treatment), a 73% mean decrease observed between the end of the first chemotherapy regimen and the onset of the second (inter-regimen) and a 69% mean decrease after both regimens.

5.3.5 ANOVA Results

Effect	ADC	FA
Comparison of distribution at short diffusion time versus long diffusion time		
Main:	F(1,476) = 0.5816, $p < 0.4461$	F(1,156) = 0.0201, $p < 0.8875$
Comparison of distribution in breast tumors pre-treatment versus post-treatment		
Main:	F(4,473) = 151.266, $p < 0.0001$*	F(4,153) = 46.0374, $p < 0.0001$*
[1]Interaction:	F(4,473) = 8.3709 , $p < 0.0001$*	F(4,153) = 0.1766, $p < 0.9502$*
[2]Post-hoc:		
	t(120) = -10.9793, $p < 0.0001$*	t(40) = -0.28053, $p < 0.7806$
	t(120) = -12.2793, $p < 0.0001$*	t(40) = -6.92558, $p < 0.0030$*
Comparison of distribution in normal fibroglandular tissue versus breast tumors		
Main:	F(1,476) = 361.257, $p < 0.0001$*	F(1,156) = 99.7259, $p < 0.0001$*
[3]Interaction:	F(1,476) = 0.1735 , $p < 0.6772$	F(1,156) = 0.0150 , $p < 0.9028$
[4]Post-hoc:		
	t(120) = 13.1907, $p < 0.0001$*	t(40) = 7.82718, $p < 0.0001$*
	t(120) = 13.9503, $p < 0.0001$*	t(40) = 8.80031, $p < 0.0001$*
	t(120) = 12.7718, $p < 0.0001$*	t(40) = 7.02972, $p < 0.0001$*
	t(120) = 14.5565, $p < 0.0001$*	t(40) = 8.08827, $p < 0.0001$*

Table 5.1 Summary of ANOVA on ADC and FA distributions.
[1] Interaction between visits and diffusion time.
[2] Pairwise contrast of pre-treatment and early treatment at short and long diffusion times.
[3] Interaction between breast tissue type and diffusion time.
[4] Pairwise contrast of normal fibroglandular tissue to breast tumor, at pre-treatment and post-treatment, at short and long diffusion time

5.4 Discussion

It was a goal of the present study to investigate whether modulating the diffusion time impacts diffusion anisotropy in breast tissue. Over the course of a diffusion experiment, protons undergo random displacements, sampling barriers such as cell membranes, organelles and so forth, in the process. Ideally, to investigate the effect of diffusion time on anisotropy in normal fibroglandular tissue, the amount of diffusing time allowed would be such that a proton could travel the maximum distance across an average sized duct, a distance of about 1 mm. It should be noted

that ductal diameter can be highly variable as ducts change over time and their dimensions differ depending on which region of the breast measurements are taken from. The time required for a proton to traverse the diameter of a duct in the absence of barriers can be estimated from the relation for the diffusion of unrestricted molecules [15]:

$$\lambda_r = \sqrt{6Dt} \tag{5.1}$$

where λ_r is the expected mean displacement, i.e. the diameter, D is the diffusion coefficient and t is time. Assuming an apparent diffusion coefficient of 2×10^{-3} mm^2/s, an average value obtained from values reported in normal fibroglandular breast tissue [16], this time is on the order of a minute. Such timing is not feasible in a normal MRI experiment due to practical considerations: the signal-to-noise ratio (SNR) is dependent on the echo time which will be prolonged by such a long diffusion time and current commercial scanners do not possess the diffusion gradient pulses necessary for such timing. The diffusion time used in the present study is reflective of these limitations. However these limitations are less relevant for detecting anisotropy in breast tumors where anisotropy is primarily determined by cell density and the average duct diameter is immaterial to anisotropy.

I hypothesized that increasing the diffusion time would increase the sensitivity of my measurements to diffusion anisotropy in breast tissue. To this end, diffusion anisotropy was measured at a short and long diffusion time in normal fibroglandular tissue and in breast tumors. I observed a trend that the distribution of fractional anisotropy, a measure of anisotropy, shifted towards higher values both in normal fibroglandular tissue and in breast tumors. However, these trends were not statistically significant. A potential explanation for the lack of statistical difference in the FA distribution of normal fibroglandular tissue at both diffusion times is that the timescale necessary to detect statistical differences in diffusion anisotropy is beyond the scope of that used in the present study. Diffusion times of 19 ms and 43 ms (a difference of 24 ms) were used in the present study. The choice of these diffusion times was informed by SNR considerations and limitations of gradient pulses available on commercial MRI scanners. Note that the shift towards higher values observed in the distribution of FA values in breast tumors was more pronounced than the shift observed in normal fibroglandular tissue (see Figure 5.5). Albeit not statistically significant, this trend is intriguing and it is worth mentioning that the present study was limited by a small sample size and the necessary exclusion of a number of data points.

Another goal of the present study was to investigate the potential for using diffusion anisotropy to characterize breast tissue and whether diffusion anisotropy could be beneficial for monitoring response to treatment. The hollowed nature of individual breast ducts suggests that diffusion might be directionally preferential within the breast ductal system, giving rise to diffusion anisotropy. Since the majority of breast carcinomas originate in the ducts of the breast, the present study investigated whether such anisotropy can be exploited to monitor response to effective treatment. I observed a wider range of values and a shift towards higher values in the distribution of the FA in normal fibroglandular breast tissue relative to breast tumors, suggesting there was more anisotropic diffusion in normal fibroglandular tissue compared with breast tumors. This is consistent with an ordered arrangement of cells in the ductal epithelium of normal fibroglandular tissue and a more random arrangement in breast tumors. While it will be necessary to confirm this finding in studies with a more robust sample size, this finding suggests

that diffusion anisotropy might be valuable in the context of treatment monitoring of breast tumors.

I observed an effect due to chemotherapy in breast tumors. The distribution of ADC values in breast tumors was shifted towards higher values after one cycle of chemotherapy suggesting an overall increase in diffusivity. Interestingly, the distribution of the FA was shifted towards lower values, suggesting less anisotropic diffusion with treatment. One theory to explain this observation is that the loss of cells following effective chemotherapy results in further disorganization of the ductal epithelium. Considering the microstructure of breast fibroglandular tissue, it is possible that in eliminating rapidly dividing cells, chemotherapy further disorganizes the epithelial layer, which would give rise to a relative decrease in anisotropy. Histology analysis will be necessary to further explore this hypothesis.

I observed a modest correlation between early change in ADC distribution and treatment response as determined by final tumor volume change. Other studies have reported stronger correlations but the present study was an explorative study with a small sample size and unforeseen challenges, namely patient motion, required the exclusion of a sizable number of data points.

To the best of my knowledge, this is the first serial study exploring diffusion anisotropy for characterizing breast tissue and examining the effects of modulating the diffusion time on diffusion anisotropy in breast tissue. Despite limitations such as a small sample size, I believe these results are very relevant for diffusion MRI measurements in the breast. My finding that diffusion anisotropy distinguishes between the distribution of normal fibroglandular tissue and breast tumors is informative for future studies of diffusion anisotropy in the breast. Additionally, my finding that a difference in diffusion time of 24 ms did not produce statistically significant differences in anisotropy measurements is relevant for future studies on the effect of anisotropy in breast tissue. Finally, my finding that diffusion anisotropy appears to decrease with chemotherapy treatment is interesting and deserving of further study.

5.5 References

1. *Breast Cancer Facts & Figures 2007-2008*. 2007, American Cancer Society, Inc.: Atlanta.
2. Lyng, H., O. Haraldseth, and E.K. Rofstad, *Measurement of cell density and necrotic fraction in human melanoma xenografts by diffusion weighted magnetic resonance imaging.* Magn Reson Med, 2000. **43**(6): p. 828-836.
3. Sugahara, T., et al., *Usefulness of diffusion-weighted MRI with echo-planar technique in the evaluation of cellularity in gliomas.* J Magn Reson, 1999. **9**(1): p. 53-60.
4. Craigmyle, M.B.L., *The Apocrine Glands and the Breast*. 1984, Chichester, New York: John Wiley & Sons.
5. Moffat, D.F. and J.J. Going, *Three dimensional anatomy of complete duct systems in human breast: pathological and developmental implications.* J Clin Pathol, 1996. **49**: p. 48-52.
6. Ramsay, D.T., et al., *Anatomy of the lactating human breast redefined with ultrasound imaging.* J. Anat, 2005. **206**(6): p. 525-534.
7. Vorherr, H., *The breast: morphology, physiology, and lactation*. 1974, New York: Academic Press.
8. Allred, D.C., S.K. Mohsin, and S.A. Fuqua, *Histological and biological evolution of human premalignant breast disease.* Endocr Relat Cancer, 2001. **8**(1): p. 47-61.
9. Burstein, H.J., et al., *Ductal carcinoma in situ of the breast.* N Engl J Med, 2004. **350**(14): p. 1430-1441.
10. Polyak, K., *Breast cancer: origins and evolution.* J Clin Invest, 2007. **117**(11): p. 3155-3163.
11. Lerwill, M., *Current practical applications of diagnostic immunohistochemistry in breast pathology.* Am J Surg Pathol, 2004. **28**(8): p. 1076-1091.
12. Basser, P.J., J. Mattiello, and D. Le Bihan, *Estimation of the effective self-diffusion tensor from the NMR spin echo* J Magn Reson Imaging, 1994. **103**(3): p. 247-254.
13. Klifa, C., et al. *Quantification of breast tissue index from MR data using fuzzy clustering*. in *IEEE EMBS*. 2004.
14. Rueckert, D., et al., *Nonrigid registration using free-form deformations: application to breast MR images.* IEEE Trans Med Imaging, 1999. **18**(8): p. 712-721.
15. Einstein, A., *On the Motion—Required by the Molecular Kinetic Theory of Heat—of Small Particles Suspended in a Stationary Liquid.* Ann Phys, 1905. **19**: p. 549-560.
16. Partridge, S.C., et al., *Menstrual cycle variation of apparent diffusion coefficients measured in the normal breast using MRI.* J Magn Reson Imaging, 2001. **14**(4): p. 433-438.

CHAPTER 6

Summary

6.1 Main Findings

In this dissertation, I have investigated the utility of MRI methods for improved monitoring of response to breast cancer treatment, in pre-clinical and clinical settings.

I characterized a pre-clinical breast tumor model to establish a baseline for subsequent measurements, where I found that the MRI parameters ADC, K^{ps}, fPV and MRI-measured tumor volume were sensitive to changes induced by treatment with gefitinib, a tyrosine kinase inhibitor.

Subsequent to the pre-clinical study, in a clinical study, I investigated the added value of diffusion MRI in the context of monitoring treatment response to chemotherapy and exploring the potential benefit of diffusion anisotropy in monitoring breast cancer treatment. I measured the diffusion tensor in normal fibroglandular breast tissue and in breast tumors before and after chemotherapy, varying the diffusion time to test the hypothesis that sensitivity to diffusion anisotropy might increase with diffusion time. I found that increasing the diffusion time by 24 ms does not result in significant changes in anisotropy but that diffusion anisotropy might be valuable in the context of treatment monitoring in breast cancer.

6.2 Reflections and Future Directions

- Limitations of this work include modest sample sizes used in the pre-clinical and clinical studies.
- In retrospect, the choice of an Echo Planar Imaging (EPI) pulse sequence for diffusion measurements in the clinical study was perhaps not ideal. EPI sequences can be loud due to rapid switching of gradient pulses. Patient discomfort resulting from the use of this sequence is suspected to have contributed to patient motion for which a sizable amount of data was disregarded.
- A challenging aspect of this work was registering dynamic contrast enhanced images to diffusion weighted images (which were acquired at a lower resolution in the interest of time). Future studies will benefit from acquiring these images at identical resolutions despite the cost in additional scan time.
- Histology analysis would be helpful to accept or reject the hypothesis postulated in section 5.4 that decreasing anisotropy with treatment might be due to re-ordering of the epithelial layer.